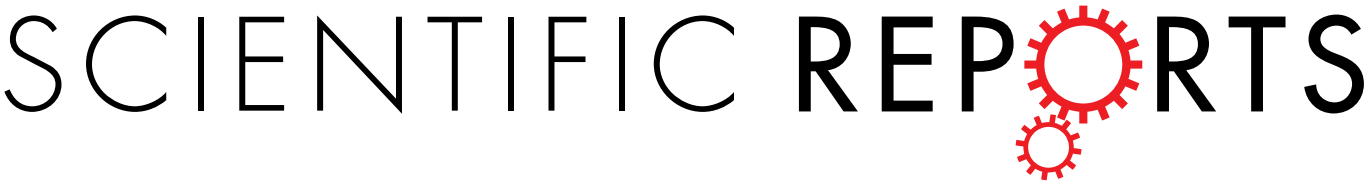

OPEN

Long Duration of Ground Motion in the Paradigmatic Valley of Mexico

V. M. Cruz-Atienza[1], J. Tago[2], J. D. Sanabria-Gómez[3], E. Chaljub[4,5], V. Etienne[6], J. Virieux[4,5] & L. Quintanar[1]

Received: 20 June 2016
Accepted: 15 November 2016
Published: 09 December 2016

Built-up on top of ancient lake deposits, Mexico City experiences some of the largest seismic site effects worldwide. Besides the extreme amplification of seismic waves, duration of intense ground motion from large subduction earthquakes exceeds three minutes in the lake-bed zone of the basin, where hundreds of buildings collapsed or were seriously damaged during the magnitude 8.0 Michoacán earthquake in 1985. Different mechanisms contribute to the long lasting motions, such as the regional dispersion and multiple-scattering of the incoming wavefield from the coast, more than 300 km away the city. By means of high performance computational modeling we show that, despite the highly dissipative basin deposits, seismic energy can propagate long distances in the deep structure of the valley, promoting also a large elongation of motion. Our simulations reveal that the seismic response of the basin is dominated by surface-waves overtones, and that this mechanism increases the duration of ground motion by more than 170% and 290% of the incoming wavefield duration at 0.5 and 0.3 Hz, respectively, which are two frequencies with the largest observed amplification. This conclusion contradicts what has been previously stated from observational and modeling investigations, where the basin itself has been discarded as a preponderant factor promoting long and devastating shaking in Mexico City.

The seismic response of the Valley of Mexico has been for many years a paradigmatic study case in earthquake seismology and engineering. After the devastation of Mexico City (MC) in 1985, when more than 15,000 people died due to a magnitude 8.0 earthquake beneath the coast of Michoacán, more than 450 km away from the city, scientists have attempted to explain site effects such as the extraordinary amplification of seismic waves and the extremely long duration of ground motion in the sedimentary basin where most of the city is located (Fig. 1). Amplification of ground motion due to local soil conditions is a well-known phenomenon. In the Valley of Mexico, spectral amplification for subduction earthquakes (i.e., with epicentral distances greater than 300 km) at soft-soil sites range from 10 to 50 at frequencies between 0.2 and 0.7 Hz with respect to hard-rock sites[1,2]. However, the hard-rock sites also experience large amplifications of about 10 due to regional site effects (quantified from attenuation relationships) associated with the volcanic arc deposits where the valley is embedded[3,4]. This means that absolute spectral amplifications in the lake-bed zone of the Valley of Mexico may reach values from 100 to 500, which are probably the largest ever reported worldwide[4].

Long-lasting ground motion in the Valley of Mexico

While the amplification of seismic waves in the Valley of Mexico has been satisfactorily explained by regional and local soil conditions[5–12], the physical reasons for the long duration of ground motion remain an open question. Initial efforts addressing this issue considered two-dimensional wave propagation models in small-basin configurations with realistic attenuation properties. Results from these exercises led to conclude that surface-waves trains generated at the edges of the basin[10,13,14] suffer a rapid decay as they propagate, and thus to discard this mechanism as a possible explanation for the long seismic records[7,15]. This conclusion invoked the existence of regional-scale effects producing the elongation of the incoming wavefield to Mexico City from subduction earthquakes, such as multipathing of seismic waves due to scatterers in the crust and surroundings of the basin[16,17], and seismic energy entrapment in both the accretionary prism near the source region and the Transmexican Volcanic Belt (TMVB)[18,19]. The interaction between the incoming wavefield and the local basin conditions may

[1]Instituto de Geofísica, Universidad Nacional Autónoma de México, Mexico. [2]Facultad de Ingeniería, Universidad Nacional Autónoma de México, Mexico. [3]Escuela de Física, Universidad Industrial de Santander, Bucaramanga, Colombia. [4]Univiversité de Grenoble Alpes, ISTerre, F-38058 Grenoble, France. [5]CNRS, ISTerre, F-38058 Grenoble, France. [6]ARAMCO, Advanced Research Center, Saudi Arabia. Correspondence and requests for materials should be addressed to V.M.C.-A. (email: cruz@geofisica.unam.mx)

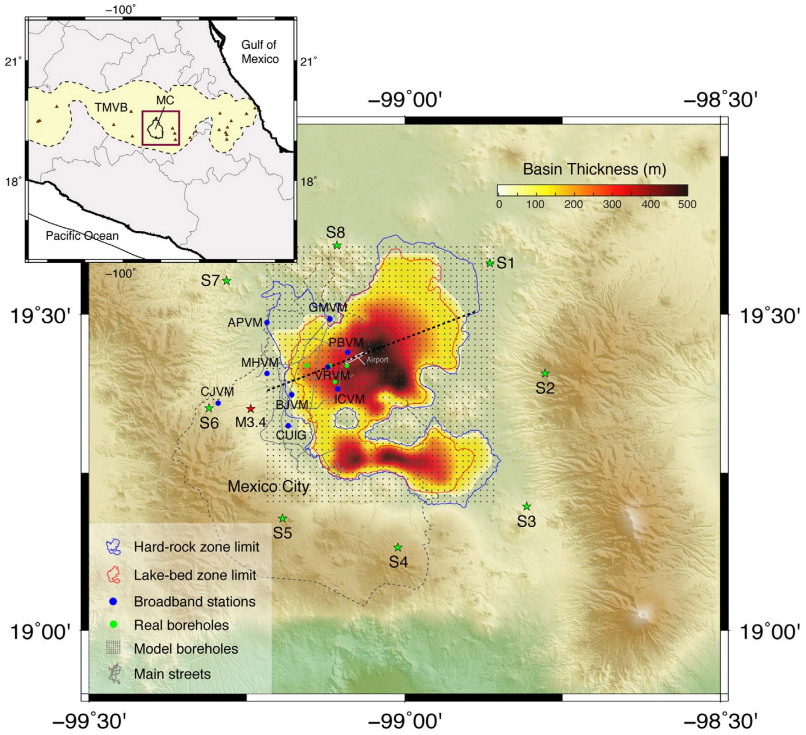

Figure 1. Topographic setting of Mexico City (MC) and the Valley of Mexico. Color scale corresponds to the basin thickness (i.e., the basin contact with the Oligocene volcanics of the Transmexican Volcanic Belt, TMVB). Stars show the epicenters for the vertical body forces applied at the free surface (green) and the magnitude 3.4 earthquake of December 1, 2014 (red). This figure has been created using the Generic Mapping Tools (GMT) Version 5.3.0, http://gmt.soest.hawaii.edu.

also elongate the ground motion when the resonant frequencies of the basin coincide with the dominant periods of the wavefield[20].

Although our current understanding of the duration of ground motion in the lake-bed zone of MC is clearly rooted in the nature of the incoming wavefield, the actual effects produced by the sedimentary basin itself have been underestimated. Figure 2a shows the seismic records ($f < 1$ Hz) of a magnitude 3.4 earthquake that occurred ~4 km below the city on December 1, 2014 (Fig. 1). These unprecedented records were possible thanks to a recently-installed permanent broadband network (blue circles) in the Valley of Mexico operated by the Servicio Sismológico Nacional (SSN). Despite the small magnitude of the event, ground motion in the basin lasted more than two minutes (e.g. at lake-bed sites VRVM, ICVM and PBVM). This can be better appreciated in the band-pass filtered signals at 0.3 Hz, where the long coda is dominated by the harmonic beating widely reported in the literature for subduction earthquakes recorded in MC[16,21]. In contrast, this beating is barely present at hard-rock sites such as CUIG and CJVM, where the motion is dominated by a single wave package with duration no longer than 20 s. This observation strongly suggests that ground motion in the lake-bed zone experiences very long durations in the absence of regional-scale effects. Local basin conditions are thus preponderant in the duration of ground shaking across the basin at frequencies where the amplification of seismic waves is the largest. The leading question of this work is thus raised about the mechanisms allowing long-lasting wave propagation within a highly dissipative sedimentary basin. Two main hypotheses may be advanced: (1) the basin incoming wavefield suffers from multiple-scattering even at a local scale, and/or (2) the sedimentary basin itself enhances sustained wave trains generation and efficient propagation.

Though certainly true, hypothesis one does not seem to have first order implications in the duration of ground motion at the lake-bed zone, as revealed by the absence of significant seismic energy in the coda of hard-rock sites (Fig. 2). On the other hand, considering the highly dissipative and fluid saturated sediments that cover large part of the basin (see next section), a plausible idea supporting hypothesis two is the efficient propagation of seismic energy in the deep basin, carried by surface-waves overtones. In this work we examine this argument based on realistic 3D wave propagation modeling to understand whether local soil conditions within the basin may explain the observed long seismic records.

A basin model for the Valley of Mexico

The Valley of Mexico is located in the southern and volcanically active part of the TMVB (Fig. 1). This region is composed by Oligocene volcanics overlaying Cretaceous limestones. On top of these formations within the valley, there are Miocene volcanics overlain by a ~100 m thick sequence of tuffs or sands, gravel and recent lava flows[11,22], averaging a thickness of ~2 km for the TMVB above the Cretaceous limestones[12,23]. Geotechnically speaking, this geologic setting corresponds to the hill zone of the valley (region outside the blue contour in Fig. 1), which may

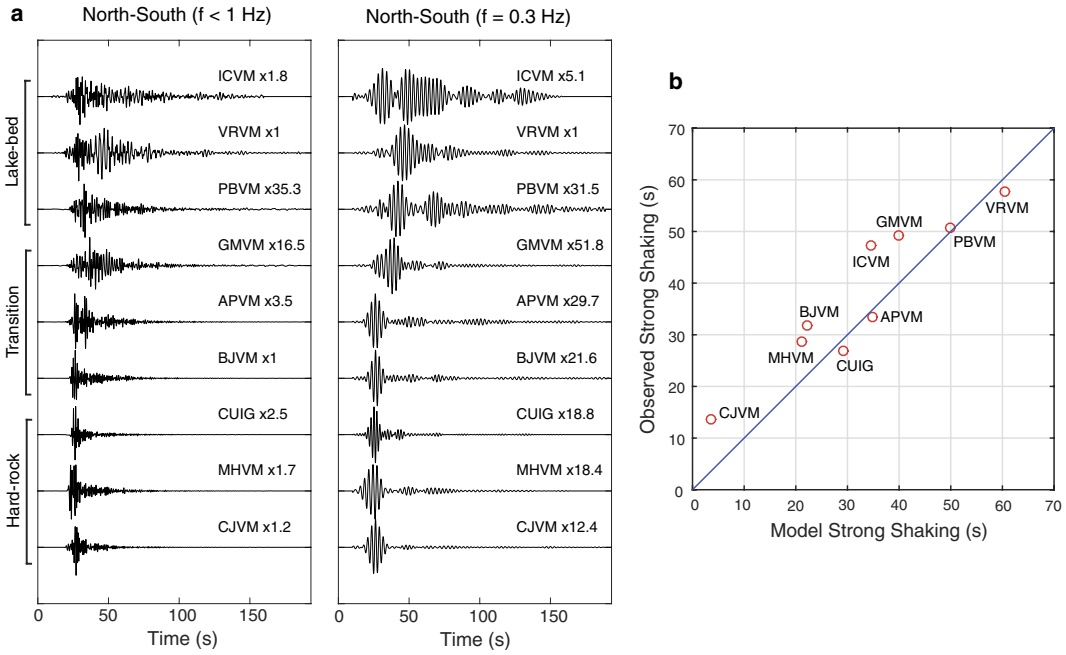

Figure 2. (**a**) Observed velocity seismograms in two different frequency bands at nine broadband seismic stations for a M3.4 earthquake with 4 km depth (see Fig. 1). Records are aligned with the P-wave arrival and scaled with the factors given for each trace. Notice the long seismic records in the lake-bed stations. (**b**) Observed and modeled durations of the strong shaking phase for f < 1 Hz. The corresponding synthetic seismograms are shown in Figure A2.

be considered hard-rock sites (e.g. CUIG, MHVM and CJVM). The stratigraphy of the MC basin is essentially the same as in the hill zone except for the absence of recent lava flows and the presence of clays with high water content of 10 to about 100 m thickness[24,25]. The basin is geotechnically known as the lake-bed zone of the valley (region within the red contour in Fig. 1) and it is where the largest amplification of ground motion is observed. The transition region in between the lake-bed and the hard-rock zones is mainly composed by alluvial deposits. The composition and thickness of the surficial clay deposits changes laterally within the basin[8,22]. However, shear-wave speed measurements on core samples from different boreholes in the lake-bed zone show extremely low values in these deposits (i.e. 30–100 m/s), with an average thickness of about 50 m[24]. Laboratory tests[26] and field estimates[27] also show that the clays are highly dissipative, with very low shear Q values ranging from 10 to 50. These observations led to a four-layer velocity model for the basin with very high Vp/Vs values on top to explain experimental data from several earthquakes[28]. We adopt this model for the lake-bed zone in our calculations (Figure A1a and Table A1).

Observations within the basin show that depths (H) to the deep, geotechnically consistent deposits are proportional to the natural vibration periods (T_0) of the sites (i.e., $H = (\beta/4)*T_0)^3$. These periods are thus proportional to the thickness of the surficial clay layers that we have assumed constant in our model. However, to confine the underlying deep-basin deposits in depth, from a large data set of natural vibration periods across the basin[2,29] and assuming an average shear-wave speed (β) of 400 m/s, we generated the bed-rock geometry shown in Fig. 1. This interface represents, in our model, the contact between the basin deposits and the Oligocene volcanics of the TMVB (i.e., fourth interface in Figure A1a). A cross section of our basin model along the dotted line of Fig. 1 is shown later in section "Dominance of surface waves overtones". Regarding the crustal structure surrounding the basin, we adopted a 1D model determined from the inversion of receiver functions at the CUIG site[30], which includes a relatively low-velocity layer on top, associated with the ~2 km thick TMVB (see Figure A1a and Table A1). To minimize numerical errors, the interfaces of the model were vertically homogenized before discretizing the model by averaging the S- and P-slownesses and densities[31] (circles in Figure A1a). The homogenization length is 50 m, which is about half of the minimum wavelength in the surficial clay layers. Using the computational method introduced in the next section we calibrated, by trial and error, the attenuation properties of the seismic model so that the durations of the intense phases of ground motions (i.e., time between 5% and 95% of the Arias intensity)[32] observed for the M3.4 earthquake in nine stations are similar to those predicted by our model assuming a 4 km depth reverse faulting below the epicenter (Figs 2b and A2), as suggested by the first P-wave arrivals. These properties, which are in accordance with laboratory and field measurements[26,27], are such that Qs = 0.3*Vs for Vs < 400 m/s and Qs = 0.1*Vs otherwise, with Qp = 2*Qs everywhere (Table A1).

Computational method for viscoelastic wave propagation

Simulating the propagation of seismic waves in extreme sedimentary basins represents a big challenge. In our seismic model for the Valley of Mexico, the S-wavelength at 1 Hz shortens from 4.8 km in the deep crust to only 50 m in the top layer of the basin during propagation. To obtain an accurate solution of the elastodynamic

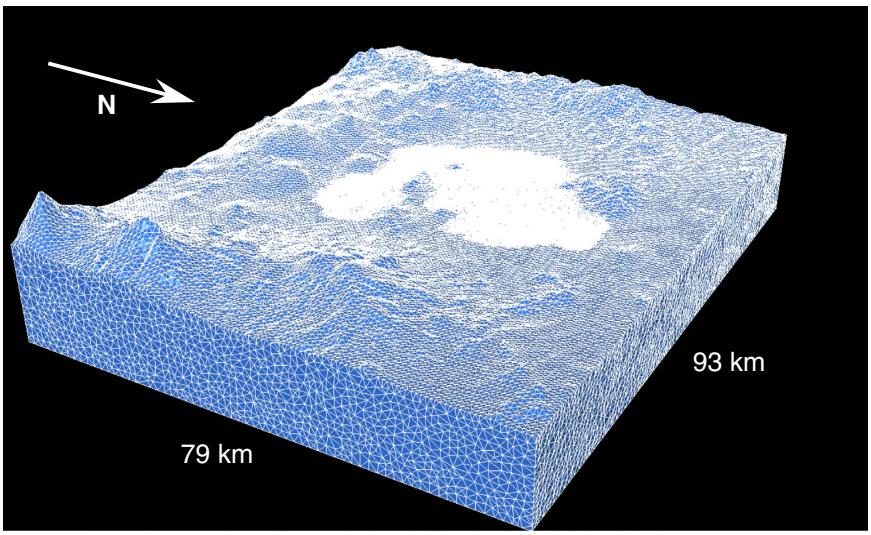

Figure 3. Top ~10 km of the unstructured tetrahedral mesh used in the study. Notice that the elements honor the basin geometry and the actual topography of the terrain (compare with Fig. 1). The mesh considered for the simulations reaches 50 km depth. This figure has been created using the TetView Linux software Version 1.0, http://wias-berlin.de/software/tetgen/tetview.html.

equations governing the propagating waves with such modulation, the numerical scheme must handle powerful capabilities to sample the wavefield efficiently in the whole simulation domain. For this reasons we have developed an hp-discontinuous Galerkin finite element method (DG-FEM) called GEODG3D that handles both unstructured domain decompositions (h-adaptivity) and different approximation orders per element in space (p-adaptivity)[33–35]. GEODG3D is an extension for viscoelastic wave propagation of a method previously introduced for elastic waves[33]. It solves the velocity-stress formulation of the visco-elastodynamic equations in three dimensions with rock quality factors, Qs and Qp, chosen to be nearly constant in the frequency range of interest (i.e., $f < 1$ Hz). For a detailed description of the viscoelastic model and the DG-FEM see Methods.

To maximize the integration time step imposed by the Courant stability criterion, GEODG3D locally adapts the elements' approximation order depending on both the elastic properties of the medium and the size of the tetrahedra (p-adaptivity) (Figure A3a). For decomposing the simulation domain in tetrahedral elements, we followed a meshing strategy that guarantees the same numerical accuracy across the whole domain[33]. Given a maximum resolvable frequency (1 Hz in this work) and starting from a regular coarse mesh, the strategy iteratively refines the elements until the accuracy criterion (i.e., 3 elements per minimum wavelength; Figure A5) is satisfied locally in at least 99.8% of the elements (h-adaptivity) (Figure A3b). Figure 3 shows the resulting mesh for the upper part of the simulation domain, where the elements are clearly adapted to both the actual topography and the extremely low velocities of the basin (compare with Fig. 1). Numerical verification (Figure A4) and convergence analysis (Figure A5) of the GEODG3D viscoelastic solver have been thoroughly done[35], finding excellent results for different international benchmark problems (see Section 3 of Methods). Table A2 provides useful numbers related to the tetrahedral mesh and discretization parameters used in all simulations of this study.

Dominance of surface waves overtones

Observational evidence for the dominance of surface waves overtones in the Valley of Mexico shows that peak displacements in the lake-bed zone between 0.3–0.5 Hz at different borehole depths (green circles in Fig. 1) for several subduction earthquakes are in accordance with theoretical eigenfunctions for the Rayleigh-waves first overtones in the basin model of Table A1[28]. These observations, which are shown later in section "Dominance of surface waves overtones", reveal that seismic energy barely decays with depth. Furthermore, surface waves dispersion diagrams generated from the correlation of ambient noise in the lake-bed zone also show the overwhelming dominance of first overtones[36]. To understand the physical reason explaining these observations and to quantify the implications in terms of ground motion duration, we first analyzed Green's functions in our 3D model of the Valley of Mexico (Fig. 3) for eight vertical forces applied at the free surface around the basin (green stars in Fig. 1). The sources radiation thus corresponds to P- and S-waves followed by a dominant Rayleigh train. In order to quantify the effect of attenuation, we performed the simulations for both the elastic and the viscoelastic cases up to 220 s in the UNAM supercomputer Miztli. Velocity snapshots for the viscoelastic simulation with source S6 are shown in Fig. 4, where amplification, diffraction and generation of surface waves at the basin edges are clearly observed.

Figure 5 shows normalized seismic profiles at 0.5 Hz with 500 m spacing for source S6 along the dashed line of Fig. 1. In the elastic case (Fig. 5a), three main pulses are observed. Two of them propagate from the basin edges with speed of ~66 m/s, and the other emerges at ~10 km of the array with a speed of 260 m/s. Considering the Rayleigh waves group-velocity dispersion curves for shallow and deep basin locations (circles in Figure A1b), speeds clearly correspond to the fundamental mode (R0) and first overtones (R1), respectively. It is striking that

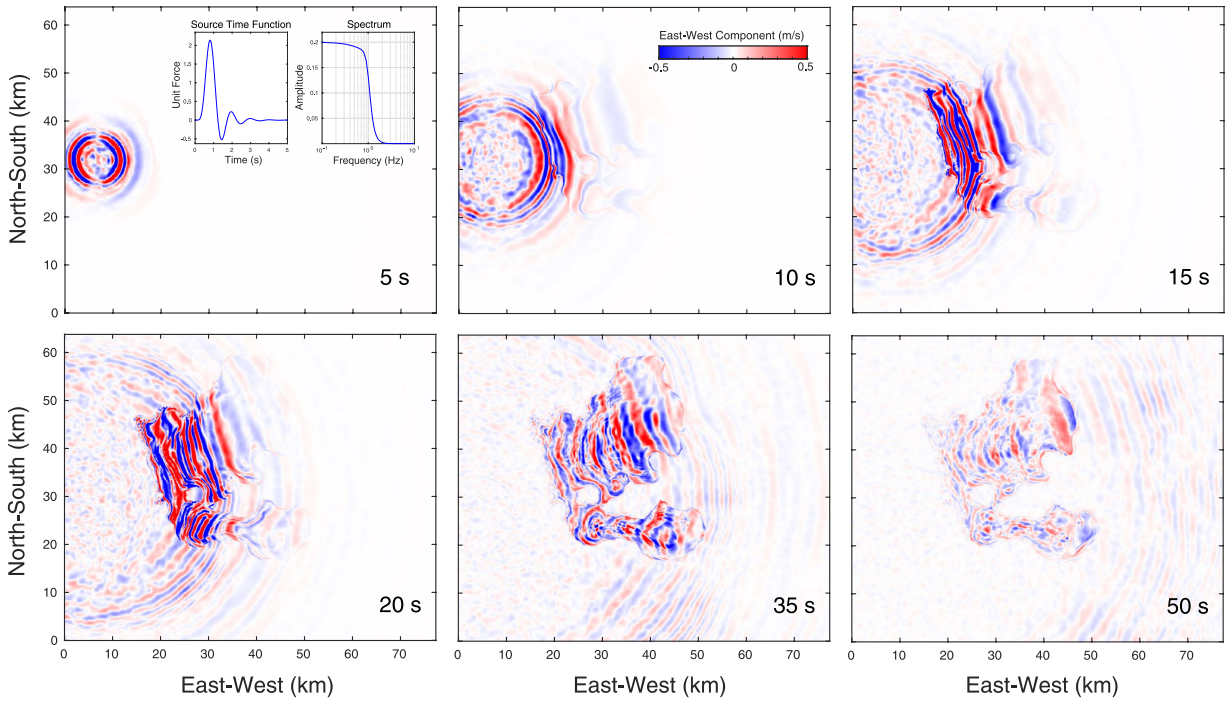

Figure 4. Snapshots of the Green's function for the vertical body force S6 (see Fig. 1) described by the inset time history with flat spectrum up to 1 Hz. Notice the topographic scattering, the generation and propagation of wave trains at different speeds within the basin, and their multiple diffractions. This figure has been created using the Matlab software Version R2016a, http://www.mathworks.com/.

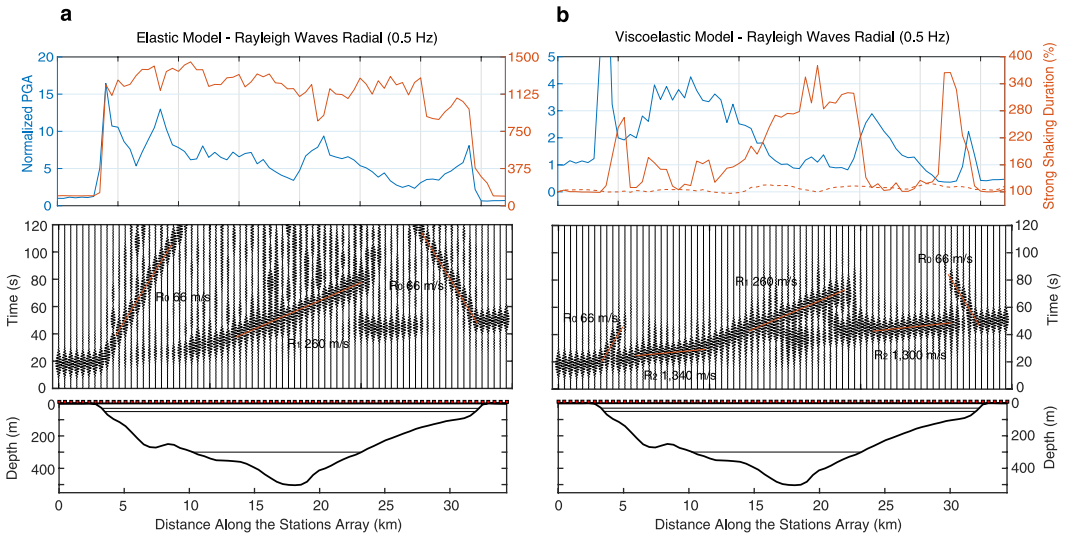

Figure 5. Seismic sections of the radial-component at 0.5 Hz for source S6 along the linear array shown in Fig. 1 for the elastic (**a**) and viscoelastic (**b**) models. A cross section of the basin model is shown at the bottom. On top, peak ground accelerations (PGAs, radial component) along the array (blue) normalized by the value at the station with smallest epicentral distance. Durations of the strong shaking phase along the array (orange) as percentages of the duration of the incoming wavefield (i.e., the duration measured at the station with smallest epicentral distance). As a reference, the dashed line indicates the durations considering only the 1D regional structure (i.e., in the absence of the basin).

even in the absence of attenuation, the first overtone dominates in the deep basin (i.e., between 10 and 23 km along the array). Unlike the elastic case, attenuation rapidly dissipates the fundamental mode and makes the overtones dominant along almost the whole array in the viscoelastic simulation (Fig. 5b). The most prominent wave train in the shallow basin regions propagates with the speed of the bedrock fundamental mode (i.e., ~1,300 m/s,

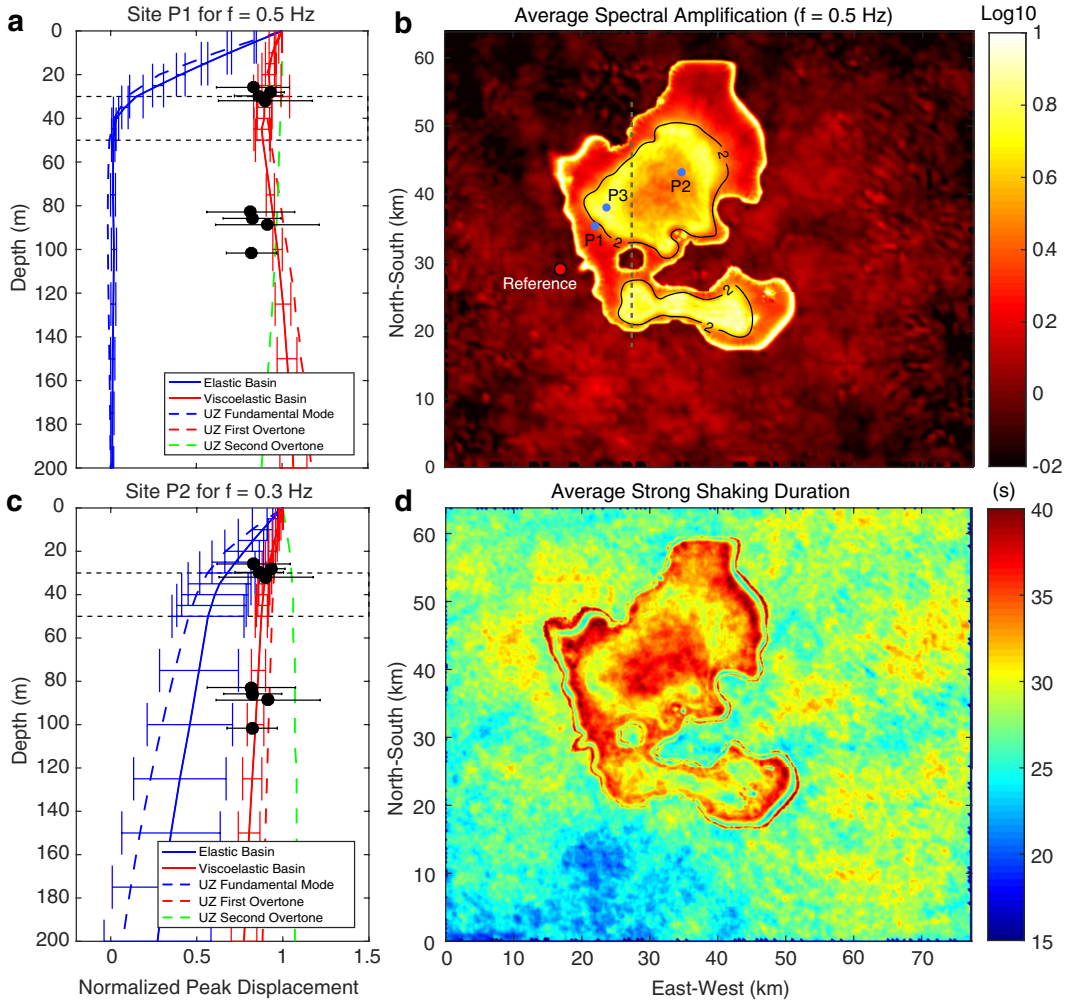

Figure 6. (**a,c**) Comparison of average eigenfunctions for the 8 sources with standard deviation bars for both elastic (blue solid) and viscoelastic (red solid) simulations at two representative sites, P1 and P2, and different frequencies. Dashed lines show theoretical eigenfunctions for the vertical component of Rayleigh waves in the model of Figure A1a (Table A1) for the fundamental mode (blue) and the first (red) and second (green) overtones. Normalized peak vertical displacements observed in different boreholes (green dots in Fig. 1) are shown with black circles and error bars (after Shapiro *et al.*, 2001). (**b**) Fourier spectral amplifications (geometric mean of both horizontal components) at 0.5 Hz with respect to the CUIG site (Fig. 1) averaged for the 8 sources. The black contour corresponds to the 2 s dominant-period. (**d**) Duration of the strong shaking phase for $f < 1$ Hz averaged for the 8 sources. This figure has been created using the Matlab software Version R2016a, http://www.mathworks.com/.

Figure A1b). This means that the incident R0 suffers a mode conversion to become the second overtone (R2) when transduced into the basin, and that such overtone dominates the ground motion at shallow regions thanks to the rapid dissipation of the basin fundamental mode, R0. Around 12 km along the array, the R1 becomes dominant when surface waves propagate from shallow to deeper parts of the basin, revealing the strong influence of the deep sediments.

A systematic analysis is necessary to conclude that overtones dominate the ground motion in the whole basin model. We thus analyzed the wavefields from the eight sources at a regular network of boreholes with 1 km spacing (gray dots in Fig. 1). From the seismograms at the network we computed and averaged synthetic eigenfunctions of Rayleigh waves for all sources in each borehole. To do so we normalized vertical displacements along the boreholes by the corresponding peak values at the free surface and at the same absolute time[28]. Figure 6a and c show the average eigenfunctions with standard deviation bars for both the elastic (blue solid lines) and viscoelastic (red solid lines) simulations at two representative sites, P1 and P2, and different frequencies. In the unrealistic elastic simulations and shallow basin regions (i.e., <250 m deep; e.g. at site P1), the energy at 0.5 Hz decays very rapidly with depth (see Figure A6a) and, consequently, the corresponding eigenfunctions fit the expected shape for the fundamental mode (dashed blue line in Fig. 6a). In contrast, in the realistic viscoelastic simulations the energy efficiently travels in depth so that the eigenfunctions fit the theoretical shape for the first and second overtones (dashed red and green lines). Something similar happens in the deep basin at 0.3 Hz (e.g., at site P2), where the elastic and viscoelastic eigenfunctions follow the expected shapes for the fundamental and

first overtone, respectively (dashed lines in Fig. 6c and Figure A6b). Although it is difficult to identify propagating pulses in the seismic profiles at 0.3 Hz (Figure A7), eigenfunctions at shallow regions reveal that ground motion is dominated by the first and/or second overtones in both the elastic and viscoelastic cases (Figure A9d). In deeper locations and 0.5 Hz, while the viscoelastic simulations are clearly dominated by the first and/or second overtones, variability of the elastic eigenfunctions reveals a contested dominance between the fundamental and higher modes (Figure A9b). In conclusion, ground motion between 0.3 and 0.5 Hz in the viscoelastic model are dominated, across the whole basin, by surface-waves overtones as data from real boreholes suggest[29] (black circles in Fig. 6a,c). The strong attenuation in the top clay layers is responsible for this propagation regime by dissipating the fundamental mode (Figure A6). RMS differences of the elastic and viscoelastic averaged eigenfunctions in the whole borehole network are shown in Figures A9a and A9c, where the shallow and deep regions of the basin are clearly distinguished by yellow colors. In those regions and frequencies, the attenuation plays a major role promoting the overtones dominance.

Implications for the duration of ground motion

Since the attenuation decreases with depth, seismic energy in the deep basin carried by overtones can propagate long distances. Basin-transduced surface waves and generation of wave trains at the basin edges, in addition to the wavefield dispersion and diffraction across the 3D structure, should then elongate the duration of ground motion. The top panels of Figs 5 and A7 show durations of the strong shaking phase for Rayleigh waves along the seismic profile for source S6. In the realistic viscoelastic model, durations grow as the basin becomes deeper, reaching values of 170–280% and 290–500% of the incoming field duration at 0.5 and 0.3 Hz, respectively. A similar situation is found for Love waves (transverse component) as shown in Figure A8, where relative durations vary as 160–280% at 0.5 Hz and 200–500% at 0.3 Hz along almost the whole array. Results for Love waves where obtained applying a 1.5 km depth double-couple strike-slip point source at location S6. In shallow regions (i.e. $<$300 m deep), peak ground accelerations (PGAs) are the largest, although significant amplification also occurs far from the source, between 22 and 28 km of the array for Rayleigh waves. As expected, amplification of single wave packages in the shallow basin region shortens the strong shaking duration. This is clear in both figures from the anti-correlation of PGA and durations along the profile. Horizontal spectral amplifications (geometric mean of both horizontal components) at 0.5 Hz with respect to the CUIG site averaged for all sources reach values larger than 10 along two ring-like regions encompassed by the 2 s dominant-period contour (Fig. 6b). These estimates are in qualitative agreement with empirical values of spectral accelerations at the same frequency[37] and suggest that regions with largest amplification may be explained by the geometry of the deep basin. Significantly larger amplifications (up to 25) are found at the lake-bed representative site P3 (Fig. 6b) around ~1.8 and ~3.2 s (Figure A10), which are two periods with similar amplification levels (with respect to CUIG) for subduction earthquakes at near by locations[2]. These results give confidence in our model predictions in terms of amplification patterns in the valley.

Average durations of horizontal strong shaking in regions with large amplification are relatively small for the reason explained above (Fig. 6d). However, durations in most regions of the basin exceed 40 s as observed in the lake-bed stations for the M3.4 earthquake (Fig. 2). Although much smaller in amplitude, ground motions at hard-rock are also long due to the scatter effect of the basin in the opposite side of the source. This is clearly seen in Figure A11, where ground motion duration inside and outside the basin is the same within the shadow-like region, proving that seismic energy recorded at hard-rock sites does not necessarily correspond to the incoming wavefield of the basin, as suggested by several authors[5,8,16]. Our simulations show that duration of ground motion is remarkably lengthened at frequencies with the largest amplification in the lake-bed (i.e., between ~0.2 and ~0.7 s) (Figs 5, A7 and A8). Long shaking duration at these frequencies may cause large structural damage in Mexico City due to the accumulation of yielding cycles that lengthen the natural vibration periods of the structures. Such mechanism makes these periods to approach those of the soil promoting structural failure, as observed during the devastating 1985 earthquake where more than three hundred 9–12 story, relatively small buildings collapsed[38,39].

In conclusion, our results demonstrate that waves overtones dominate the ground motion in the lake-bed zone of the Valley of Mexico and that this propagation regime strongly contributes to the elongation of intense shaking (i.e., duration of both Rayleigh and Loves waves longer than 170% and 290% of the incoming field duration at 0.5 and 0.3 Hz, respectively) at frequencies where the largest amplification is observed. The bedrock fundamental mode is transduced into the basin and converted into overtones (first and second modes) that dominate the ground motion. The structure of the deep basin is responsible for this mechanism, proving that local basin conditions remarkably increase the duration of strong motion in the lake-bed despite the highly dissipative surficial sediments. Our results imply that duration of the incoming wavefield from subduction earthquakes should be significantly shorter than the observed duration in the lake-bed zone. This conclusion contradicts what has been previously stated from observational and theoretical studies considering the ground motion at hard-rock sites as the basin incoming wavefield. The contradiction can be explained if the seismic coda at those sites is dominated by multiple-scattered local waves generated at the basin, as suggested by our simulations.

References

1. Singh, S. K. *et al.* The Mexico Earthquake of September 19, 1985—A Study of Amplification of Seismic Waves in the Valley of Mexico with Respect to a Hill Zone Site. *Earthquake Spectra* **4,** 653–673, doi: 10.1193/1.1585496 (1988).
2. Reinoso, E. & Ordaz, M. Spectral Ratios for Mexico City from Free-Field Recordings. *Earthquake Spectra* **15,** 273–295, doi: 10.1193/1.1586041 (1999).
3. Singh, S. K., Mena, E. & Castro, R. Some aspects of source characteristics of the 19 September 1985 Michoacan earthquake and ground motion amplification in and near Mexico City from strong motion data. *Bulletin of the Seismological Society of America* **78,** 451–477 (1988).

4. Ordaz, M. & Singh, S. K. Source spectra and spectral attenuation of seismic waves from Mexican earthquakes, and evidence of amplification in the hill zone of Mexico City. *Bulletin of the Seismological Society of America* **82,** 24–43 (1992).
5. Sánchez-Sesma, F., Chávez-Pérez, S., Suárez, M., Bravo, M. A. & Pérez-Rocha, L. E. The Mexico Earthquake of September 19, 1985—On the Seismic Response of the Valley of Mexico. *Earthquake Spectra* **4,** 569–589, doi: 10.1193/1.1585491 (1988).
6. Campillo, M., Bard, P. Y., Nicollin, F. & Sánchez-Sesma, F. The Mexico Earthquake of September 19, 1985—The Incident Wavefield in Mexico City during the Great Michoaca´n Earthquake and Its Interaction with the Deep Basin. *Earthquake Spectra* **4,** 591–608, doi: :10.1193/1.1585492 (1988).
7. Bard, P. Y., Campillo, M., Chávez-García, F. J. & Sánchez-Sesma, F. The Mexico Earthquake of September 19, 1985—A Theoretical Investigation of Large- and Small-scale Amplification Effects in the Mexico City Valley. *Earthquake Spectra* **4,** 609–633, doi: 10.1193/1.1585493 (1988).
8. Seed, H. B., Romo, M. P., Sun, J. I., Jaime, A. & Lysmer, J. The Mexico Earthquake of September 19, 1985—Relationships Between Soil Conditions and Earthquake Ground Motions. *Earthquake Spectra* **4,** 687–729, doi: 10.1193/1.1585498 (1988).
9. Kawase, H. & Aki, K. A study on the response of a soft basin for incident S, P, and Rayleigh waves with special reference to the long duration observed in Mexico City. *Bulletin of the Seismological Society of America* **79,** 1361–1382 (1989).
10. Chávez-García, F. J. & Bard, P.-Y. Site effects in Mexico City eight years after the September 1985 Michoacán earthquakes. *Soil Dynamics And Earthquake Engineering* **13,** 229–247 (1994).
11. Singh, S. K. *et al.* Is there truly a "hard" rock site in the Valley of Mexico? *Geophysical Research Letters* **22,** 481–484, doi: 10.1029/94GL03298 (1995).
12. Shapiro, N. M. *et al.* Surface-wave propagation across the Mexican Volcanic Belt and the origin of the long-period seismic-wave amplification in the Valley of Mexico. *Geophysical Journal International* **128,** 151–166, doi: 10.1111/j.1365-246X.1997.tb04076.x (1997).
13. Bard, P.-Y. & Bouchon, M. The seismic response of sediment-filled valleys. Part 2. The case of incident P and SV waves. *Bulletin of the Seismological Society of America* **70,** 1921–1941 (1980).
14. Kawase, H. Site effects on strong ground motions. *International Handbook of Earthquake and Engineering Seismology*, Part B, Lee, W. H. K. & Kanamori, H. (eds.) Academic Press, London, 1013–1030 (2003).
15. Chávez-García, F. J., Ramos-Martínez, J. & Romero-Jiménez, E. Surface-wave dispersion analysis in Mexico City. *Bulletin of the Seismological Society of America* **85,** 1116–1126 (1995).
16. Singh, S. K. & Ordaz, M. On the origin of long coda observed in the lake-bed strong-motion records of Mexico City. *Bulletin of the Seismological Society of America* **83,** 1298–1306 (1993).
17. Barker, J. S., Campillo, M., Sánchez-Sesma, F. J., Jongmans, D. & Singh, S. K. Analysis of wave propagation in the Valley of Mexico from a dense array of seismometers. *Bulletin of the Seismological Society of America* **86,** 1667–1680 (1996).
18. Shapiro, N. M., Olsen, K. B. & Singh, K. On the duration of seismic motion incident onto the Valley of Mexico for subduction zone earthquakes. *Geophysical Journal International* **151,** 501–510, doi: 10.1046/j.1365-246X.2002.01789.x (2002).
19. Cárdenas-Soto, M. & Chávez-García, F. J. Regional Path Effects on Seismic Wave Propagation in Central Mexico. *Bulletin of the Seismological Society of America* **93,** 973–985, doi: 10.1785/0120020083 (2003).
20. Chávez-García, F. J. & Salazar, L. Strong Motion in Central Mexico: A Model Based on Data Analysis and Simple Modeling. *Bulletin of the Seismological Society of America* **92,** 3087–3101, doi: 10.1785/0120010231 (2002).
21. Bodin, P., Gomberg, J., Singh, S. K. & Santoyo, M. Dynamic deformations of shallow sediments in the Valley of Mexico, Part I: Three-dimensional strains and rotations recorded on a seismic array. *Bulletin of the Seismological Society of America* **87,** 528–539 (1997).
22. Pérez-Cruz, G. Estudio sismológico de reflexión del subsuelo de la ciudad de México. *MSc Thesis, Faculty of Engineering, Universidad Nacional Autónoma de México, Mexico* (1988).
23. Havskov, J. & Singh, S. K. Shallow crustal structure below Mexico City. *Geofísica Internacional* **17,** 222–229 (1977-78).
24. Singh, S. K., Santoyo, M., Bodin, P. & Gomberg, J. Dynamic deformations of shallow sediments in the Valley of Mexico, Part II: Single-station estimates. *Bulletin of the Seismological Society of America* **87,** 540–550 (1997).
25. Ovando-Shelley, E., Romo, M. P. & Ossa, A. The sinking of Mexico city: Its effects on soil properties and seismic response. *Soil Dynamics and Earthquake Engineering* **24,** 333–343 (2007).
26. Romo, M. P. & Ovando-Shelley, E. Modeling the dynamic behavior of Mexican clays. *Eleventh World Conf. Earthquake Engineering, Acapulco, Mexico* no. 1028 (1996).
27. Jongmans, D., Demanet, D., Horrent, C., Campillo, M. & Sánchez-Sesma, F. J. Dynamic soil parameters determination by geophysical prospecting in Mexico City: implication for site effect modeling. *Soil Dynamics and Earthquake Engineering* **15,** 549–559 (1996).
28. Shapiro, N. M., Singh, S. K., Almora, D. & Ayala, M. Evidence of the dominance of higher-mode surface waves in the lake-bed zone of the Valley of Mexico. *Geophysical Journal International* **147,** 517–527, doi: 10.1046/j.0956-540x.2001.01508.x (2001).
29. Lermo, J., Rodríguez, M. & Singh, S. K. The Mexico Earthquake of September 19, 1985—Natural Period of Sites in the Valley of Mexico from Microtremor Measurements and Strong Motion Data. *Earthquake Spectra* **4,** 805–814, doi: 10.1193/1.1585503 (1988).
30. Cruz-Atienza, V. M., Iglesias, A., Pacheco, J. F., Shapiro, N. M. & Singh, S. K. Crustal Structure below the Valley of Mexico Estimated from Receiver Functions. *Bulletin of the Seismological Society of America* **100,** 3304–3311, doi: 10.1785/0120100051 (2010).
31. Chaljub, E. *et al.* 3-D numerical simulations of earthquake ground motion in sedimentary basins: testing accuracy through stringent models. *Geophysical Journal International* **201,** 90–111, doi: 10.1093/gji/ggu472 (2015).
32. Arias, A. A measure of earthquake intensity. *Hansen RJ (ed) Seismic design for nuclear power plants*. MIT Press, Cambridge, Massachusetts, 438–483 (1970).
33. Etienne, V., Chaljub, E., Virieux, J. & Glinsky, N. An hp-adaptive discontinuous Galerkin finite-element method for 3-D elastic wave modelling. *Geophysical Journal International* **183,** 941–962, doi: 10.1111/j.1365-246X.2010.04764.x (2010).
34. Tago, J., Cruz-Atienza, V. M., Virieux, J., Etienne, V. & Sánchez-Sesma, F. J. A 3D hp-adaptive discontinuous Galerkin method for modeling earthquake dynamics. *Journal of Geophysical Research: Solid Earth* **117,** n/a-n/a, doi: 10.1029/2012JB009313 (2012).
35. Tago, J. Modelado de la dinámica de la fuente sísmica y de la propagación de ondas viscoelásticas con el método de Galerkin discontinuo. *Ph.D. Thesis, Universidad Nacional Autónoma de México, Mexico*, p. 250 (2012).
36. Rivet, D., Campillo, M., Sanchez-Sesma, F., Shapiro, N. M. & Singh, S. K. Identification of surface wave higher modes using a methodology based on seismic noise and coda waves. *Geophysical Journal International* **203,** 856–868, doi: 10.1093/gji/ggv339 (2015).
37. Singh, S., Iglesias, A., Ordaz, M., Pérez-Campos, X. & Quintanar, L. Estimation of Ground Motion in Mexico City from a Repeat of the M∼7.0 Acambay Earthquake of 1912. *Bulletin of the Seismological Society of America* **101,** 2015–2028 (2011).
38. Hall, J. F. & Beck, J. L. Structural damage in Mexico City. *Geophysical Research Letters* **13,** 589–592, doi: 10.1029/GL013i006p00589 (1986).
39. Beck, J. L. & Hall, J. F. Factors contributing to the catastrophe in Mexico City during the earthquake of September 19, 1985. *Geophysical Research Letters* **13,** 593–596, doi: 10.1029/GL013i006p00593 (1986).

Acknowledgements

We thank Michel Campillo for fruitful and enlightening discussions, Shri K. Singh for his comments and criticism on the manuscript, and Pierre-Yves Bard and Francisco Sánchez-Sesma for their advices in the results interpretation. We also thank Vladimir Kostoglodov for helpful layout and editorial advises, Eduardo Reinoso

for the basin isoperiod map and useful information and Arturo Cárdenas for the installation and maintenance of the seismic network of the Valley of Mexico. The HPC-GA grant of the Marie Curie International Research Staff Exchange Scheme has supported this work under call FP7-PEOPLE-2011-IRSES. The calculations presented in this article were performed using the supercomputer Miztli of the National Autonomous University of Mexico (UNAM) under grant number SC16-1-IR-87 and the Froggy platform from the CIMENT HPC center of Grenoble Alpes University which is supported by the Rhône-Alpes region (grant CPER07_13 CIRA), the OSUG@2020 labex (reference ANR10 LABX56) and the Equip@Meso project (reference ANR-10-EQPX-29-01). J.D.S-G. acknowledges the financial support from the Universidad Industrial de Santander of Colombia and the Seismology Department of UNAM for its hospitality during the time of this project.

Author Contributions

V.M.C.-A. designed the study, performed the computational simulations, interpreted the results and wrote the manuscript. J.T. implemented and adapted the viscoelastic solver and interpreted the results. J.D.S.-G. generated the numerical mesh, performed the computational simulations and interpreted the results. E.C. interpreted the results and performed the basin model homogenization. V.E. generated the numerical mesh. J.V. interpreted the results. L.Q. provided the seismic data. All authors contributed with discussions and improvements of the manuscript.

Additional Information

Supplementary information accompanies this paper at http://www.nature.com/srep

Competing financial interests: The authors declare no competing financial interests.

How to cite this article: Cruz-Atienza, V. M. *et al.* Long Duration of Ground Motion in the Paradigmatic Valley of Mexico. *Sci. Rep.* **6**, 38807; doi: 10.1038/srep38807 (2016).

Publisher's note: Springer Nature remains neutral with regard to jurisdictional claims in published maps and institutional affiliations.

Supplementary Information

of "Long Duration of Ground Motion in the Paradigmatic Valley of Mexico"

V.M. Cruz-Atienza, J. Tago, J.D. Sanabria-Gómez, E. Chaljub,
V. Etienne, J. Virieux and L. Quintanar

August 26, 2016

In this section we introduce the mathematical and computational models used to simulate the wave propagation in the Valley of Mexico. First, we introduce the model for a viscoelastic rheology and how we couple the corresponding constitutive relationship with the equation of motion to get the hyperbolic system describing the viscoelastic wave propagation. Then, we introduce the system discretization following a discontinuous Galerkin strategy, and present the computational model verification and convergence analysis based on different international benchmark problems. We also include all tables and supplementary figures referred in the main text of the manuscript.

1 Viscoelastic model for waves propagation

The stress-strain constitutive relationship in an isotropic viscoelastic medium can be defined as

$$\begin{aligned}\sigma_{ij}(t) &= \delta_{ij}\delta_{kl}\int_{-\infty}^{t}\lambda(t-\tau)\partial_t\epsilon_{kl}(\tau)d\tau \\ &\quad +(\delta_{ik}\delta_{jl}+\delta_{il}\delta_{jk})\int_{-\infty}^{t}\mu(t-\tau)\partial_t\epsilon_{kl}(\tau)d\tau,\end{aligned} \tag{1}$$

where $\sigma_{ij}(t)$ is the stress tensor, $\lambda(t)$ and $\mu(t)$ are the Lamé relaxation functions and $\epsilon_{kl}(t)$ is the strain tensor.

To avoid the unaffordable computation of the time convolutions in equation (1), for each Lamé relaxation function we will model the viscoelastic rheology as a *Generalized Maxwell Body* (GMB-EK) with n *Maxwell Bodies* (MB) and 1 *Hooke Body* (HB) connected in parallel[4]. In the frequency domain, the relaxation functions can be written as

$$\lambda(\omega) = \lambda_U\left(1-\sum_{l=1}^{n}Y_l^{\lambda}\frac{\omega_l}{\omega_l+i\omega}\right) \tag{2}$$

$$\mu(\omega) = \mu_U\left(1-\sum_{l=1}^{n}Y_l^{\mu}\frac{\omega_l}{\omega_l+i\omega}\right), \tag{3}$$

where λ_U and μ_U are the unrelaxed Lamé parameters that correspond to the instantaneous elastic response of the viscoelastic material, Y_l^{λ} and Y_l^{μ} are the anelastic coefficients and ω_l are the relaxation frequencies for the l^{th} MB. The anelastic coefficients, Y_l^{λ} and Y_l^{μ}, gather some physical properties of the propagation medium[11] and its computation will be explain in Section 1.1.

We use the inverse Fourier transformation to express the Lamé relaxation functions (equations (2) and (3)) in the

time domain, so that convolutions in equation (1) may be written as:

$$\int_{-\infty}^{t} \lambda(t-\tau)\partial_t \epsilon_{kl}(\tau)d\tau = \lambda_U \epsilon_{kl} - \lambda_U \sum_{m=1}^{n} Y_m^{\lambda} \zeta_m^{kl}(t) \tag{4}$$

$$\int_{-\infty}^{t} \mu(t-\tau)\partial_t \epsilon_{kl}(\tau)d\tau = \mu_U \epsilon_{kl} - \mu_U \sum_{m=1}^{n} Y_m^{\mu} \zeta_m^{kl}(t), \tag{5}$$

where we define the anelastic functions as

$$\zeta_m^{kl}(t) = \omega_m \int_{-\infty}^{t} \epsilon_{kl}(\tau) \exp^{-\omega_m(t-\tau)} d\tau \qquad m = 1, \cdots, n \quad k, l \in \{1, 2, 3\}, \tag{6}$$

and, because of the exponential term in equation (6), the time evolution of the anelastic functions can be associated with their own ODE[8]:

$$\partial_t \zeta_m^{kl}(t) + \omega_m \zeta_m^{kl}(t) = \omega_m \epsilon_{kl}(t) \qquad m = 1, \cdots, n \quad k, l \in \{1, 2, 3\}. \tag{7}$$

By substituting equations (4) and (5) into equation (1) our constitutive relationship becomes

$$\begin{aligned} \sigma_{ij}(t) &= \delta_{ij}\delta_{kl}\lambda_U \epsilon_{kl}(t) + (\delta_{ik}\delta_{jl} + \delta_{il}\delta_{jk})\mu_U \epsilon_{kl}(t) \\ &\quad - \sum_{m=1}^{n} (\delta_{ij}\delta_{kl}\lambda_U Y_m^{\lambda} \zeta_m^{kl}(t) + (\delta_{ik}\delta_{jl} + \delta_{il}\delta_{jk})\mu_U Y_m^{\mu} \zeta_m^{kl}(t)). \end{aligned} \tag{8}$$

To avoid having the physical properties involved in the fluxes computation[1] (see Section 2), we define the stress vector as $\vec{\sigma} = (\omega, \omega', \omega'', \sigma_{xy}, \sigma_{xz}, \sigma_{yz})^t$ with $\omega = \frac{1}{3}(\sigma_{xx}+\sigma_{yy}+\sigma_{zz})$, $\omega' = \frac{1}{3}(2\sigma_{xx}-\sigma_{yy}-\sigma_{zz})$ and $\omega'' = \frac{1}{3}(-\sigma_{xx}+2\sigma_{yy}-\sigma_{zz})$. This change of variable allows to express equation (8) in the following matrix form as

$$\Lambda \vec{\sigma} = \sum_{\theta \in \{x,y,z\}} \partial_\theta \mathcal{N}_\theta \vec{u} - \sum_{l=1}^{n} \mathcal{A}_l \vec{\zeta_l} \tag{9}$$

where $\vec{u} = (u_x, u_y, u_z)^t$ is the displacement vector and $\vec{\zeta_l} = (\zeta_l^{xx}, \zeta_l^{yy}, \zeta_l^{zz}, \zeta_l^{xy}, \zeta_l^{xz}, \zeta_l^{yz})^t$ is the anelastic function vector for the l^{th} MB. Matrix $\Lambda = \text{diag}[3/(3\lambda_U + 2\mu_U), (3/2\mu_U), 3/(2\mu_U), 1/\mu_U, 1/\mu_U, 1/\mu_U]$, which gathers the physical properties of the medium, is given by the unrelaxed Lamé parameters, λ_U and μ_U, and $\mathcal{N}_\theta$ are constant real matrices defined as

$$\mathcal{N}_x = \begin{pmatrix} 1 & 2 & -1 & 0 & 0 & 0 \\ 0 & 0 & 0 & 1 & 0 & 0 \\ 0 & 0 & 0 & 0 & 1 & 0 \end{pmatrix}^T \quad \mathcal{N}_y = \begin{pmatrix} 0 & 0 & 0 & 1 & 0 & 0 \\ 1 & -1 & 2 & 0 & 0 & 0 \\ 0 & 0 & 0 & 0 & 0 & 1 \end{pmatrix}^T \quad \mathcal{N}_z = \begin{pmatrix} 0 & 0 & 0 & 0 & 1 & 0 \\ 0 & 0 & 0 & 0 & 0 & 1 \\ 1 & -1 & -1 & 0 & 0 & 0 \end{pmatrix}^T.$$

Matrix $\mathcal{A}$, associated with the anelastic term of equation (8), is given by

$$\mathcal{A}_l = \begin{bmatrix} \mathcal{A}_l^1 & \mathcal{A}_l^1 & \mathcal{A}_l^1 & 0 & 0 & 0 \\ 2\mathcal{A}_l^2 & -\mathcal{A}_l^2 & -\mathcal{A}_l^2 & 0 & 0 & 0 \\ -\mathcal{A}_l^2 & 2\mathcal{A}_l^2 & -\mathcal{A}_l^2 & 0 & 0 & 0 \\ 0 & 0 & 0 & 2\mathcal{A}_l^2 & 0 & 0 \\ 0 & 0 & 0 & 0 & 2\mathcal{A}_l^2 & 0 \\ 0 & 0 & 0 & 0 & 0 & 2\mathcal{A}_l^2 \end{bmatrix}, \tag{10}$$

where $\mathcal{A}_l^1 = \frac{3\lambda_U Y_l^{\lambda} + 2\mu_U Y_l^{\mu}}{3\lambda_U + 2\mu_U}$ and $\mathcal{A}_l^2 = Y_l^{\mu}$.

To obtain the first part of the hyperbolic system of partial differential equations governing the propagation of viscoelastic waves, we just applied the time derivative to equation (9):

$$\Lambda\partial_t\vec{\sigma} = \sum_{\theta\in\{x,y,z\}} \partial_\theta \mathcal{N}_\theta \vec{v} - \sum_{l=1}^{n} \mathcal{A}_l \vec{\xi}_l, \tag{11}$$

where $\vec{v} = \partial_t\vec{u} = (v_x, v_y, v_z)^t$ is the velocity vector, and $\vec{\xi}_l = \partial_t\vec{\zeta}_l = (\xi_l^{xx}, \xi_l^{yy}, \xi_l^{zz}, \xi_l^{xy}, \xi_l^{xz}, \xi_l^{yz})^t$, is the time derivative of the anelastic functions vector $\vec{\zeta}_l$ that for simplicity, we will still call the anelastic function vector. Then the ODE associated with $\vec{\xi}_l$ is given by

$$\partial_t\vec{\xi}_l + \omega_l\vec{\xi}_l = \omega_l \sum_{\theta\in\{x,y,z\}} \partial_\theta \mathcal{O}_\theta \vec{v}, \tag{12}$$

where

$$\mathcal{O}_x = \begin{bmatrix} 1 & 0 & 0 & 0 & 0 & 0 \\ 0 & 0 & 0 & 0.5 & 0 & 0 \\ 0 & 0 & 0 & 0 & 0.5 & 0 \end{bmatrix}^T \quad \mathcal{O}_y = \begin{bmatrix} 0 & 0 & 0 & 0.5 & 0 & 0 \\ 0 & 1 & 0 & 0 & 0 & 0 \\ 0 & 0 & 0 & 0 & 0 & 0.5 \end{bmatrix}^T \quad \mathcal{O}_z = \begin{bmatrix} 0 & 0 & 0 & 0 & 0.5 & 0 \\ 0 & 0 & 0 & 0 & 0 & 0.5 \\ 0 & 0 & 1 & 0 & 0 & 0 \end{bmatrix}^T. \tag{13}$$

To complete the hyperbolic system and keep track of the time-varying velocity field, we incorporate the equation of motion. This equation can be written in matrix form[1] as

$$\rho\partial_t\vec{v} = \sum_{\theta\in\{x,y,z\}} \partial_\theta \mathcal{M}_\theta \vec{\sigma} + \vec{f}, \tag{14}$$

where ρ is the medium density, $\vec{f}$ is the external force vector and $\mathcal{M}_\theta$ are constant real matrices defined as

$$\mathcal{M}_x = \begin{pmatrix} 1 & 1 & 0 & 0 & 0 & 0 \\ 0 & 0 & 0 & 1 & 0 & 0 \\ 0 & 0 & 0 & 0 & 1 & 0 \end{pmatrix} \quad \mathcal{M}_y = \begin{pmatrix} 0 & 0 & 0 & 1 & 0 & 0 \\ 1 & 0 & 1 & 0 & 0 & 0 \\ 0 & 0 & 0 & 0 & 0 & 1 \end{pmatrix} \quad \mathcal{M}_z = \begin{pmatrix} 0 & 0 & 0 & 0 & 1 & 0 \\ 0 & 0 & 0 & 0 & 0 & 1 \\ 1 & -1 & -1 & 0 & 0 & 0 \end{pmatrix}.$$

Thus, equations (11) and (14) constitute the hyperbolic system fully describing the viscoelastic wave propagation.

1.1 Computation of the anelastic coefficients

The computation of the anelastic coefficients, Y_l^λ and Y_l^μ, in equations (2) and (3) is done such that the quality factors, Q_φ, for $\varphi \in \{\lambda, \mu\}$, are approximated over a frequency range of interest. The inverse of the quality factor is defined for each Lamé relaxation function (equations (2) and (3)) as

$$Q_\varphi^{-1}(\omega) = \frac{\mathrm{Im}\varphi(\omega)}{\mathrm{Re}\varphi(\omega)} = \sum_{l=1}^{n} \frac{\omega_l\omega + Q^{-1}(\omega)\omega_l^2}{\omega_l^2 + \omega^2} Y_l^\varphi \qquad \varphi \in \{\lambda, \omega\}. \tag{15}$$

To approximate a nearly constant $Q_\varphi(\omega)$ in a given frequency range, we set the relaxation frequencies ω_l in the frequency range of interest with a logarithmically equidistant spacing[4]. A constant Q has been proved to be a good approximation for most geophysical applications[9]. Nonetheless, the following procedure can also be applied for any frequency dependency of Q[10]. Once the relaxation frequencies are spread along the frequency range, we used a least square method to determine the anelastic coefficients in equation (15) that better fit the function $Q_\varphi(\omega)$.

In practice, seismologists describe the rocks anelastic dissipation through the quality factors Q_α and Q_β associated with the P- and S- waves, respectively. After computing their corresponding coefficients Y_l^α and Y_l^β, we can compute

those related with the Lamé parameters using the transformations

$$Y_l^{\lambda} = \left(1 + \frac{2\mu}{\lambda}\right) Y_l^{\alpha} - \frac{2\mu}{\lambda} Y_l^{\beta} \qquad \text{and} \qquad Y_l^{\mu} = Y_l^{\beta}. \tag{16}$$

For our simulations, we have considered three MB (i.e., three relaxation frequencies) to approximate constant Q_α and Q_β in the frequency range [0.01 5.0] Hz, which is a reasonable choice for our modeling purposes. The more relaxation frequencies we consider the better is the approximation of the given function $Q_\varphi(\omega)$. However, it is important to notice that increasing the amount of relaxation frequencies implies a significant increment in the memory storage requirements and computational time.

2 hp-Discontinuous Galerkin method

Before solving the hyperbolic system given by equations (11) and (14), we first need to decompose the physical domain, Ω, into K elements, so that

$$\Omega \simeq \Omega_h = \sum_{i=1}^{K} D_i \tag{17}$$

where each D_i is a straight-sided tetrahedron whose union constitutes a geometrically conforming mesh .

We approximate the velocity and stress vectors in every tetrahedron, D_i $\forall i \in \{1, \ldots, K\}$, using a nodal interpolation[6] as

$$\hat{\vec{v}}_i(\vec{x}, t) = \sum_{j=1}^{d_i} \vec{v}_{i_j}(\vec{x}_j, t)\varphi_{i_j}(\vec{x}) \tag{18}$$

$$\hat{\vec{\sigma}}_i(\vec{x}, t) = \sum_{j=1}^{d_i} \vec{\sigma}_{i_j}(\vec{x}_j, t)\varphi_{i_j}(\vec{x}), \tag{19}$$

where $\vec{x} \in D_i$, t is the time and d_i is the number of nodes supporting the interpolation Lagrangian polynomial basis functions, φ_{i_j}, associated to the j-node located at $\vec{x}_j$.

Using the nodal interpolations (18) and (19), we can apply a discontinuous Galerkin approach[5] to equations (11) and (14) and get

$$\begin{aligned} \rho_i(\mathcal{I}_3 \otimes \mathcal{K}_i)\frac{\vec{v}_i^{n+\frac{1}{2}} - \vec{v}_i^{n-\frac{1}{2}}}{\Delta t} &= -\sum_{\theta \in \{x,y,z\}} (\mathcal{M}_\theta \otimes \mathcal{E}_{i\theta})\vec{\sigma}_i^n \\ &\quad + \frac{1}{2}\sum_{k \in N_i} [(\mathcal{P}_{ik} \otimes \mathcal{F}_{ik})\vec{\sigma}_i^n + (\mathcal{P}_{ik} \otimes \mathcal{G}_{ik})\vec{\sigma}_k^n] \end{aligned} \tag{20}$$

$$\begin{aligned} (\Lambda_i \otimes \mathcal{K}_i)\frac{\vec{\sigma}_i^{n+1} - \vec{\sigma}_i^n}{\Delta t} &= -\sum_{\theta \in \{x,y,z\}} (\mathcal{N}_\theta \otimes \mathcal{E}_{i\theta})\vec{v}_i^{n+\frac{1}{2}} - \sum_{l=1}^{n} (\mathcal{A}_{i_l} \otimes \mathcal{K}_i)\vec{\xi}_{i_l}^{n+\frac{1}{2}} \\ &\quad + \frac{1}{2}\sum_{k \in N_i} \left[(\mathcal{Q}_{ik} \otimes \mathcal{F}_{ik})\vec{v}_i^{n+\frac{1}{2}} + (\mathcal{Q}_{ik} \otimes \mathcal{G}_{ik})\vec{v}_k^{n+\frac{1}{2}}\right] \end{aligned} \tag{21}$$

where the matrices involved are: the mass matrix

$$(\mathcal{K}_i)_{rj} = \int_{V_i} \varphi_{i_r}\varphi_{i_j} dV \qquad j, r \in [1, d_i],$$

the stiffness matrix

$$(\mathcal{E}_{i\theta})_{rj} = \int_{V_i} (\partial_\theta \varphi_{i_r}) \varphi_{i_j} dV \qquad j, r \in [1, d_i] \qquad \theta \in \{x, y, z\},$$

the flux matrices

$$\begin{aligned} (\mathcal{F}_{ik})_{rj} &= \int_{S_{ik}} \varphi_{i_r} \varphi_{i_j} dS \qquad j, r \in [1, d_i] \\ (\mathcal{G}_{ik})_{rj} &= \int_{S_{ik}} \varphi_{i_r} \varphi_{k_j} dS \qquad r \in [1, d_i] \qquad j \in [1, d_k]. \end{aligned}$$

and the auxiliary flux matrices

$$\begin{aligned} \mathcal{P}_{ik} &= \sum_{\theta \in \{x,y,z\}} n_{ik_\theta} \mathcal{M}_\theta \\ \mathcal{Q}_{ik} &= \sum_{\theta \in \{x,y,z\}} n_{ik_\theta} \mathcal{N}_\theta, \end{aligned}$$

where $\mathcal{I}_3$ is the 3x3 identity matrix, $\otimes$ represent the tensor product, and n_{ik_θ} is the component along the θ axis of the unit normal vector $\vec{n}_{ik}$ of the element face S_{ik} which points from the i- to the k-element.

The size of these matrices depends on the order of the polynomial basis used for the nodal interpolation. The flux terms of the i^{th}-tetrahedron are computed following a non-dissipative centered scheme with its N_i adjacent elements. Besides, thanks to the change of variable previously introduced, the fluxes of equation (21) do not involve the physical properties of the neighboring elements but only their velocity fields.

In our method, we have implemented P0, P1 and P2 (i.e. constant, linear and quadratic) approximation orders that can be individually assigned to each tetrahedron D_i depending on its characteristic size and medium properties (i.e., p-adaptivity). Staggered time integration is performed through a second-order explicit leap-frog scheme, which allows the alternation of velocities and stresses during computation. The order of approximation used for time integration matches the highest approximation order for the spatial interpolation (*i.e.* P2).

To solve the ODE's governing the anelastic functions (12), we approximate these functions using a nodal interpolation and the same Galerkin approach introduced before for equations (11) and (14), to get

$$\begin{aligned} (\mathcal{I}_6 \otimes \mathcal{K}_i) \frac{\vec{\xi}_{i_l}^{n+\frac{1}{2}} - \vec{\xi}_{i_l}^{n-\frac{1}{2}}}{\Delta t} &= -\omega_l \left((\mathcal{I}_6 \otimes \mathcal{K}_i) \vec{\xi}_{i_l}^{n-\frac{1}{2}} + \sum_{\theta \in \{x,y,z\}} (\mathcal{O}_\theta \otimes \mathcal{E}_{i\theta}) \vec{v}_i^{n-\frac{1}{2}} \right) \\ &\quad + \omega_l \frac{1}{2} \sum_{k \in N_i} \left[(\mathcal{R}_{ik} \otimes \mathcal{F}_{ik}) \vec{v}_i^{n-\frac{1}{2}} + (\mathcal{R}_{ik} \otimes \mathcal{G}_{ik}) \vec{v}_k^{n-\frac{1}{2}} \right] \end{aligned} \tag{22}$$

where $\mathcal{R}_{ik} = \sum_{\theta \in \{x,y,z\}} n_{ik_\theta} \mathcal{O}_\theta$. It is important to notice that the discontinuous Galerkin approximation used for the ODE's allows us to honour the p-adaptivity of the scheme.

In order to achieve good accuracy for P2 elements, the unstructured model discretization must warranty 3 tetrahedra per minimum wavelength[5] (see Figure A5). On the other hand, the scheme stability is given by an heuristic criterion[7] given by

$$\Delta t < \min_i \left(\frac{1}{2k_i + 1} \cdot \frac{2r_i}{\alpha_i} \right) \tag{23}$$

where r_i is the radius of the sphere inscribed in the element indexed by i, α_i is the $P-$wave velocity in the element and k_i is the polynomial degree used in the element.

Our Discontinuous Galerkin Finite Element Method (DG-FEM) (i.e., the GEODG3D code) thus has two main features that make it a very flexible and powerful numerical tool. One is the h-adaptivity, which allows working with unstructured tetrahedral meshes geometrically adapted to the physical properties of the medium and the free surface topography, so that the accuracy criterion is satisfied locally (Figures 3a and A3b). The other is the p-adaptivity, that allows choosing the most convenient order of approximation per tetrahedron to relax as much as possible the stability condition (i.e., to maximize the integration time step). A nice example of p-adaptivity is given in Figure A3a, where the elements right below the basin, which have a very little characteristic size and relatively high wave speeds, are low approximation order (i.e., P1 or P0). This numerical approach was developed in recent years during the PhD thesis of Tago (2012)[12], where more methodological and numerical details are provided.

3 Model verification and convergence

To verify the correctness of the solutions yielded by the GEODG3D code, we solved two international benchmarks problems. Solutions were compared with those from AXITRA[2], a semi-analytical discrete wave number method. The benchmarks correspond to the elastic and viscoelastic versions of the Layer Over an Homogeneous half-space problems, LOH1 and LOH3, respectively[3].

For the LOH3 benchmark, the viscoelastic moduli were exactly the same in both the AXITRA and GEODG3D simulations. This choice allows quantifying approximation errors associated only to the implementation of the attenuation model for a given number of relaxation mechanisms and thus for the same $Q(\omega)$ functions. In this benchmark problem, the top layer is 1000 m thick and the physical properties of the whole model are given in Table A3. We approximated the frequency-independent quality factors Q_α and Q_β with three relaxation mechanisms. Receivers are located in the free surface ($z = 0$) with positions relative to the epicenter ($x \rightarrow$ North and $y \rightarrow$ East) given in Table A4. A double-couple point source is located 2000 m below the free surface with all components of its moment tensor equal to zero except $M_{xy} = M_{yx}$, with moment value $M_0 = 10^{18}\ Nm$. The Moment rate time history is a Gaussian pulse given by

$$\frac{1}{t_r\sqrt{\pi}} \exp \frac{-(t-t_0)^2}{t_r^2}, . \tag{24}$$

where t is the time, $t_r = 0.05\ s$ is the rise time and $t_0 = 0.25\ s$ is the origin time. The source spectrum is almost flat up to 10 Hz so all the frequencies below have almost the same amplitude. Solutions should be compared up to 5.0 Hz.

All solutions were computed using P2 elements in the physical domain, approximately ten P1 elements in the Convolutional Perfectly Matched Layer (CPML)[5] region and free surface boundary conditions on top of the model. The characteristic size of the tetrahedra used for both the structured and the unstructured meshes was 100 m, as suggested in the benchmarks descriptions[3]. This choice is convenient for our method since the number of elements per minimum wavelength, n_λ, is about three, which corresponds to the accuracy criterion for our method[5] (see Figure A5).

Figure A4 shows the comparison of the three velocity components in the farthest three receivers (*i.e.* located about 32 times the minimum wavelength from the epicenter) using an unstructured mesh. The time series were filtered using a two-pass four-pole Butterworth filter in the frequency band $[1 - 5]\ Hz$. The agreement between solutions is excellent (i.e., error of about 1.2%).

We performed a convergence analysis of the GEODG3D method based on both the elastic (LOH1) and the viscoelastic (LOH3) benchmarks considering structured and unstructured meshes. The Normalized Root Mean Square (NRMS)

function was used to quantify the error between our solutions and the AXITRA reference solutions. This function is given by

$$NRMS(v_\theta^{DG-FEM}, v_\theta^{AXITRA}) = \frac{\sqrt{(\sum_{i=1}^{n}(v_{\theta_i}^{DG-FEM} - v_{\theta_i}^{AXITRA})^2)/n}}{max(v_\theta^{AXITRA}) - min(v_\theta^{AXITRA})}, \tag{25}$$

where n is the length of the seismograms vectors and $\theta \in \{x, y, z\}$. Components with no signals were excluded in the NRMS computation. For the rest of receivers we computed the NRMS in the three velocity components and averaged them to have a single misfit value.

Figure A5 presents NRMS values computed for the following four simulation cases: 1) the LOH1 benchmark with structured mesh, 2) the LOH1 benchmark with unstructured mesh, 3) the LOH3 benchmark with structured mesh and 4) the LOH3 benchmark with unstructured mesh. NRMS values are reported as a function of the number of elements per minimum wavelength, n_λ, associated with the cutoff frequency of 5 Hz. Linear regressions are also plotted in the log-log scale. The resulting slopes give the convergence rates of the solutions with respect to n_λ. For the unstructured viscoelastic case (i.e., for conditions similar to our simulations in the Valley of Mexico) the convergence rate is 2.98.

Four main conclusions detach from Figure A5: 1) viscoelastic solutions are systematically better than the elastic ones no matter we use structured or unstructured meshes; 2) the convergence rate of both viscoelastic and elastic solutions is virtually the same and depends on the kind of mesh we use; 3) the convergence rate is significantly higher in unstructured meshes no matter we solve the elastic or viscoelastic equations (*i.e.* convergence rate about 1.8 times higher); and 4) numerical errors are lower than 2% and 1.2% in structured and unstructured meshes, respectively, provided that $n_\lambda >= 3$ no matter we solve the elastic or viscoelastic equations.

References

1. Benjemaa, M., N. Glinsky-Olivier, V. M. Cruz-Atienza, and J. Virieux, 3-d dynamic rupture simulations by a finite volume method, *Geophys. J. Int.*, *178*(1), doi:10.1111/j.1365-246X.2009.04088.x, 2009.

2. Bouchon, M., and O. Coutant, Calculation of synthetic seismograms in a laterally varying medium by the boundary element-discrete wavenumber method, *Bull. Seismol. Soc. Am.*, *84*, 1869–1881, 1994.

3. Day, S. M., J. Bielak, D. Dreger, R. Graves, S. Larsen, K. Olsen, and A. Pitarka, Test of 3D elastodynamics codes: Final report for lifelines project 1A02, *Tech rept.*, Pacific Earthquake Engineering Research Center, Berkeley, California, 2003.

4. Emmerich, H., and M. Korn, Incorporation of attenuation into time-domain computations of seismic wave fields, *Geophysics*, *52*(9), doi:10.1190/1.1442386, 1987.

5. Etienne, V., E. Chaljub, J. Virieux, and N. Glinsky, An hp-adaptive discontinuous Galerkin finite-element method for 3-D elastic wave modelling, *Geophys. J. Int.*, *183*(2), doi:10.1111/j.1365-246X.2010.04764.x, 2010.

6. Hesthaven, J. S., and T. Warburton (Eds.), *Nodal Discontinuous Galerkin Methods: Algorithms, Analysis and Applications*, 1st ed., 515 pp., Springer, 2008.

7. Kaser, M., and M. Dumbser, A highly accurate discontinuous Galerkin method for complex interfaces between solids and moving fluids, *Geophysics*, *73*(3), 23–35, 2008.

8. Kristek, J., and P. Moczo, Seismic-Wave Propagation in Viscoelastic Media with Material Discontinuities: A 3d Fourth-Order Staggered-Grid Finite-Difference Modeling, *Bull. Seism. Soc. Am.*, *93*, doi:10.1785/0120030023, 2003.

9. Liu, H. P., D. L. Anderson, and H. Kanamori, Velocity dispersion due to anelasticity; implications for seismology and mantle composition, *Geophys. J. Roy. Astr. Soc.*, *47*, 41–58, 1976.

10. Liu, P., and R. J. Archuleta, Efficient Modeling of Q for 3D Numerical Simulation of Wave Propagation, *Bull. Seismol. Soc. Am.*, *96*(4), 1352–1358, 2006.

11. Moczo, P., and J. Kristek, On the rheological models used for time-domain methods of seismic wave propagation, *Geophys. Res. Lett.*, *32*(L01306), doi:10.1029/2004GL021598, 2005.

12. Tago, J., Modelado de la dinámica de la fuente sísmica y de la propagación de ondas viscoelásticas con el método de Galerkin discontinuo, Ph.D. thesis, UNAM, Mexico, 2012.

Table A1 Velocity structure considered in this study. Green shaded layers correspond to those inside the 3D basin geometry shown in Figure 1. Blue shaded layers correspond to the 1D structure where the basin is embedded. Thicknesses indicated with stars correspond to the deepest point of the basin. They vary depending on the basin geometry.

H (km)	Vp (km/s)	Vs (km/s)	Rho (gr/cm^3)	Qp	Qs
0.03	0.8	0.05	2.0	30.0	15.0
0.02	1.2	0.1	2.0	60.0	30.0
0.25	2.0	0.4	2.05	80.0	40.0
0.25*	2.5	0.8	2.05	160.0	80.0
1.42*	2.70	1.56	2.20	312.0	156.0
2.34	5.51	3.18	2.53	636.0	318.0
10.97	6.00	3.46	2.69	692.0	346.0
27.62	6.68	3.86	2.91	772.0	386.0
∞	8.31	4.80	3.43	960.0	480.0

Table A2 Numerical information of a typical viscoelastic simulation. The UNAM supercomputing platform Miztli has 40 Gb Infiniband interconextion and processors Intel Xeon E5-2670 with frequency of 2.6 to 3.3 GHz.

Maximum resolved frequency	1 Hz
Size of the simulation domain	93.3 x 79.7 x 50.3 km
Length of the CPML layer	8 km
Number of mesh elements	12.25 million
Elements within the basin	97.04 %
P0 elements	10.41 %
P1 elements	12.85 %
P2 elements	76.75 %
Minimum element size	0.49 m
Maximum element size	737 m
Integration time step	0.00036 s
Number of time steps	514,995
Number of parallel processors	512
Computing elapsed time	23.7 hr

Table A3: Medium parameters of the LOH3 benchmark

	α (m/s)	β (m/s)	ρ (kg/m^3)	Q_α	Q_β
layer	4000	2000	2600	120	40
halfspace	6000	3464	2700	180	80

Table A4: Receivers location of the LOH1 and LOH3 benchmarks

Receiver	1	2	3	4	5	6	7	8	9
x (m)	0	0	0	490	3919	7348	577	4612	8647
y (m)	693	5543	10392	490	3919	7348	384	3075	5764

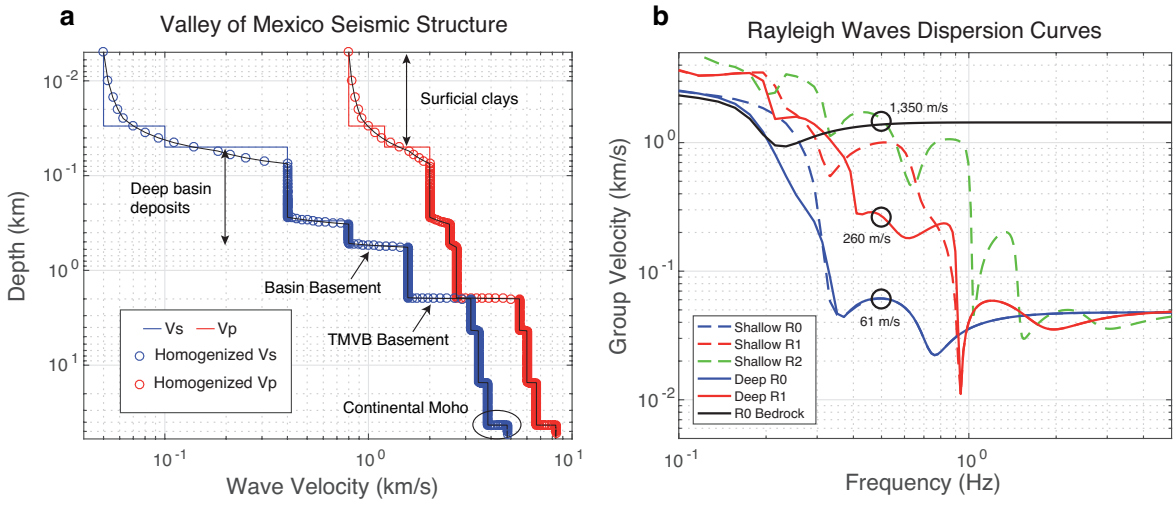

Figure A1 (a) Velocity structure used in the numerical model (see Table A1). Depth of the basin basement varies in space according to the basin thickness shown in Figure 1. Circles show the homogenized velocity structure used for the model discretization. (b) Rayleigh waves dispersion curves for the vertical component of the fundamental (R0, blue) and first overtone (R1, red) at shallow (250 m thick; dashed) and deep (500 m thick; solid) basin sites.

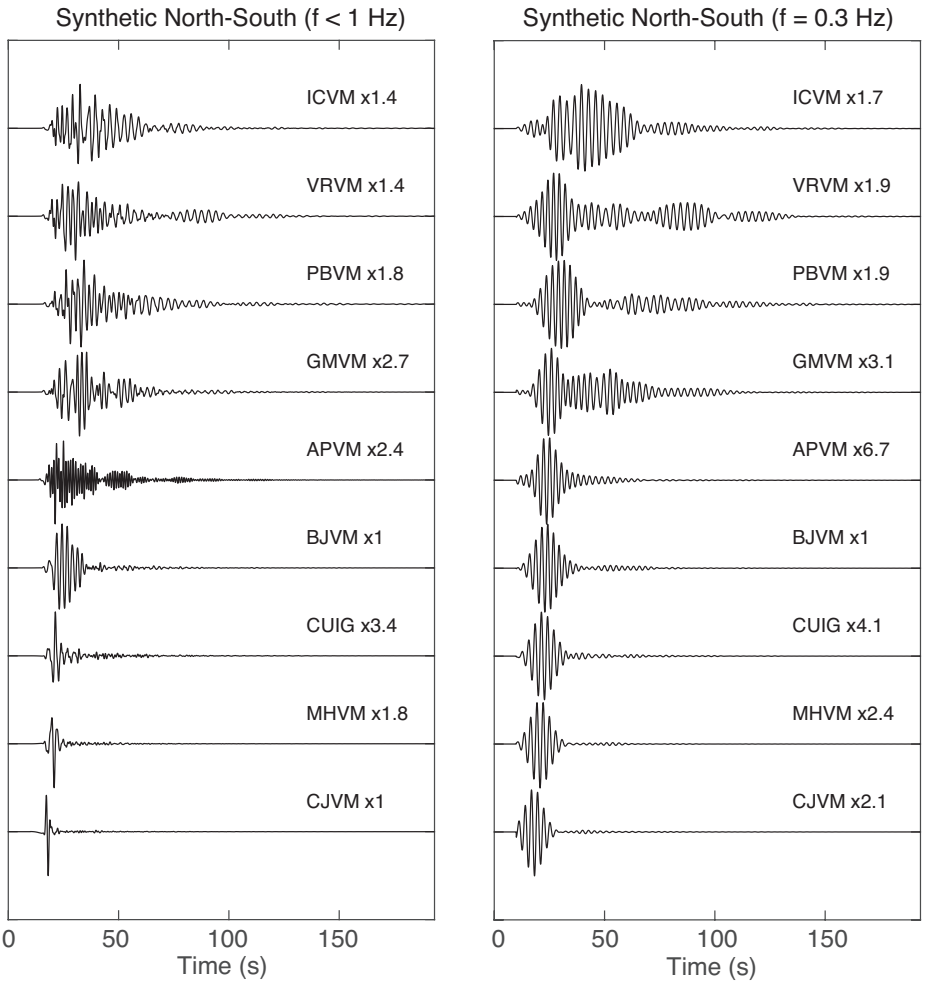

Figure A2 Synthetic velocity seismograms computed at nine broadband stations for the M3.4 earthquake with 4 km depth (Figure 1). The source is a vertical dip-slip dislocation with strike to the north and source time function shown in the inset of Figure 4. Records are aligned with the P-wave arrival. Durations of the strong shaking phases for f < 1 Hz are compared with real observations in Figure 1b.

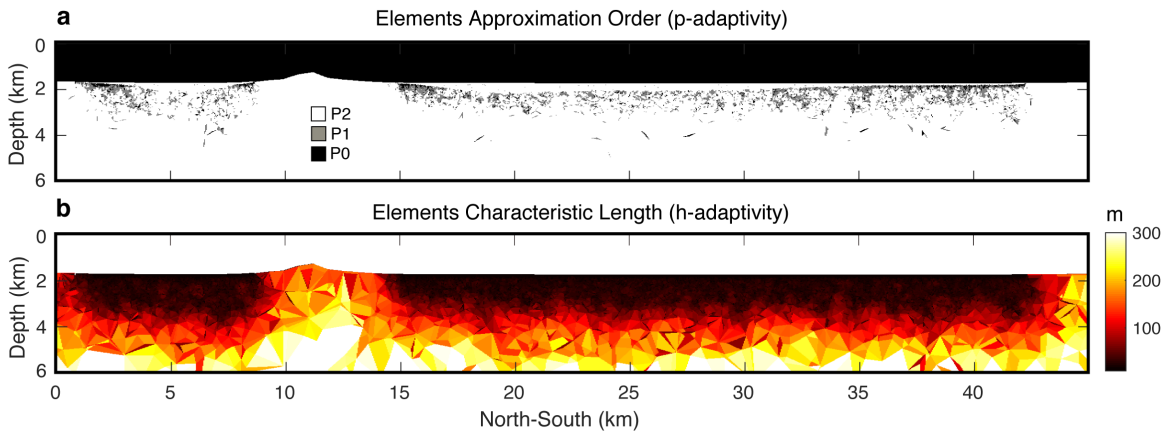

Figure A3 (a) Cross-section of the discrete model along the dashed line of Figure 6b. The distribution of the elements approximation order (i.e., p-adaptivity) is indicated with three different colors. Notice the concentration of low-order elements right below the interface with highest impedance contrasts (i.e., below the shallower basin regions close to its borders). (b) Same cross-section showing the tetrahedral mesh refinement within the basin (h-adaptivity).

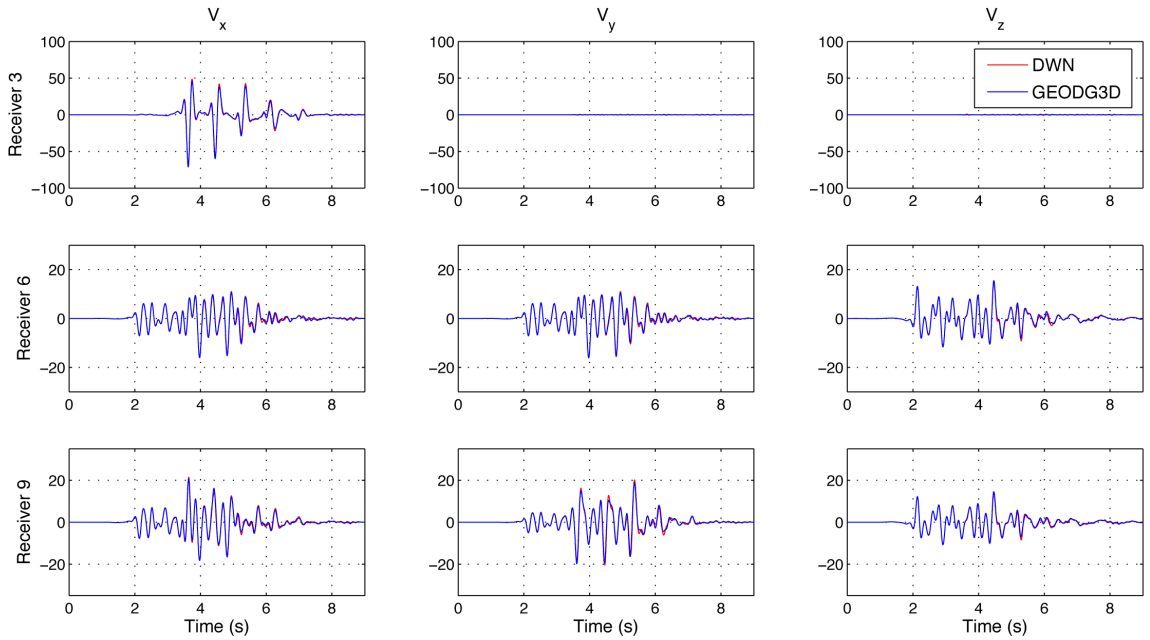

Figure A4 Comparison of synthetic seismograms (bandpass filtered between 1 and 5 Hz) computed with the Discontinuous Galerkin GEODG3D method (blue) and the Discrete Wave Number method (DWN, red) for the viscoelastic benchmark "Layer Over a Halfspace 3" (LOH3) of the Southern California Earthquake Center (SCEC) described by Day et al. (2003). Both solutions were computed with exactly the same viscoelastic modulus for three relaxation mechanisms so the signals misfit only responds to numerical approximation errors. The GEODG3D solution was computed using a P2 unstructured mesh with characteristic size of 100 m. The three receivers are located at distances from the source of about 32 times the minimum wavelength.

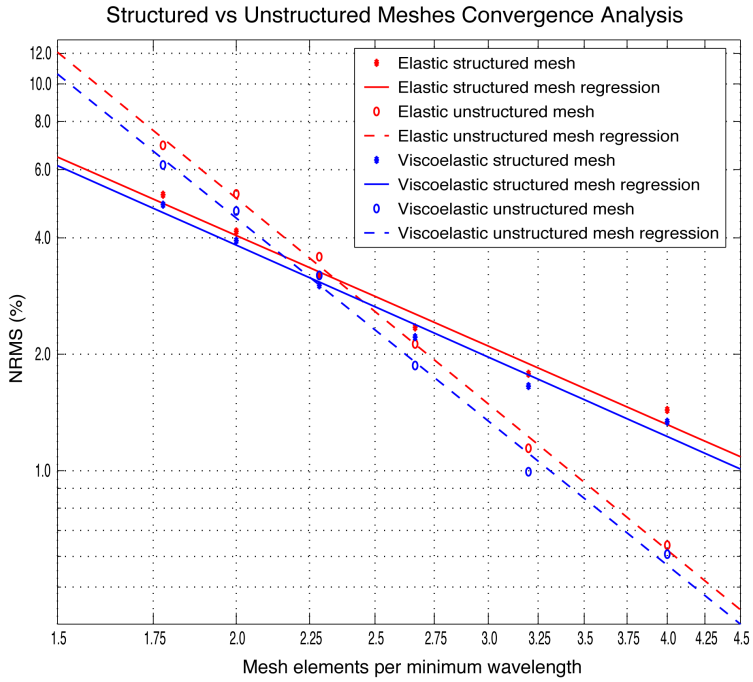

Figure A5 Convergence analysis for GEODG3D elastic (red) and viscoelastic (blue) methods considering structured (solid) and unstructured (dashed) meshes. Problems used were the LOH1 and LOH3 (Day et al., 2003) taking the DWN solutions as references. Viscoelastic solutions are always better that the elastic. Convergence rate in unstructured meshes (slope of 2.98) is significantly higher than the corresponding value for structured meshes (slope of 1.64). This is due to the numerical anisotropy induced by the regularity of elements in the structured mesh.

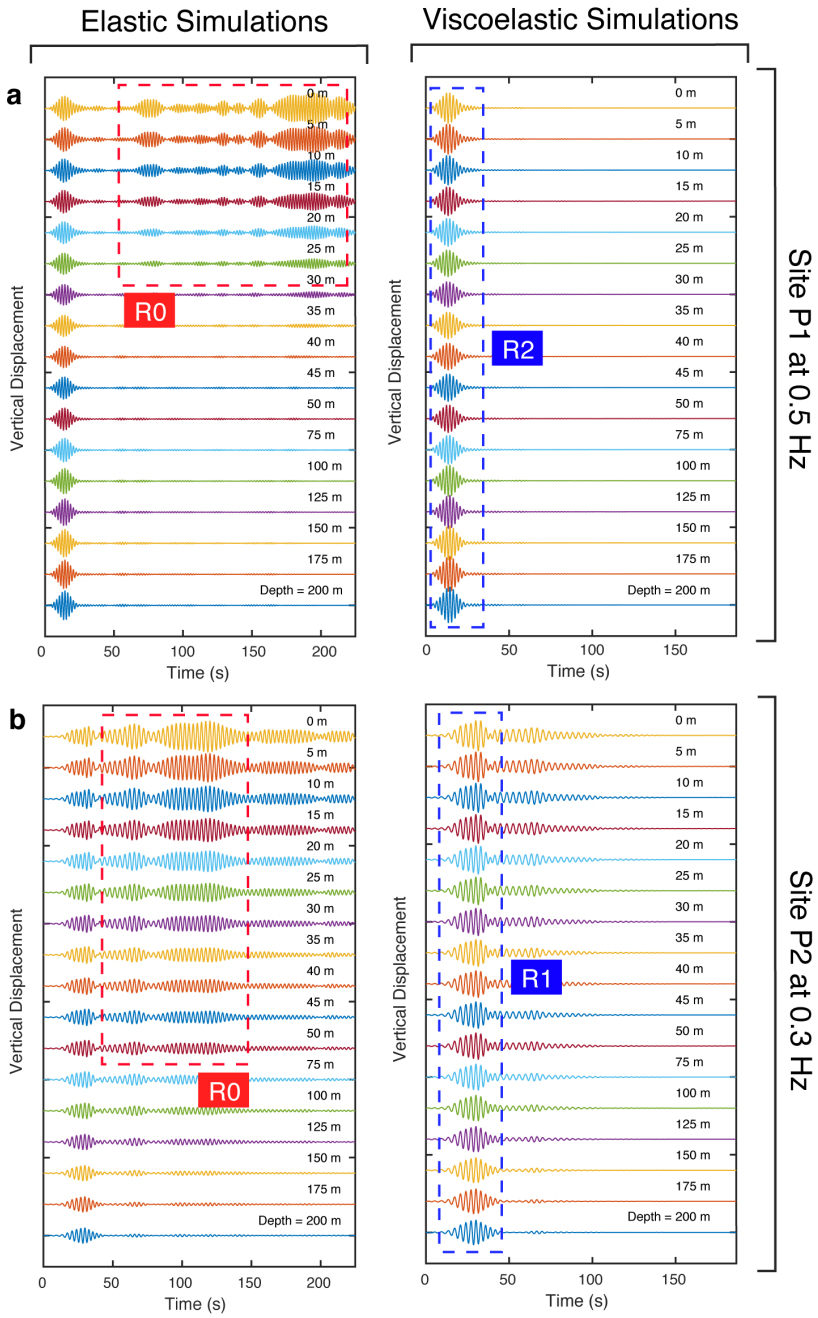

Figure A6 Synthetic borehole seismograms at sites P1 and P2 (see Figure A9) for two different frequencies. While the energy of the fundamental mode (R0) decays rapidly with depth (red rectangles), that of the first and second overtones (R1 and R2) persists along the entire depth of the borehole. Compare the amplitudes of the wave packages with the eigenfunctions of Figures 6a and 6c.

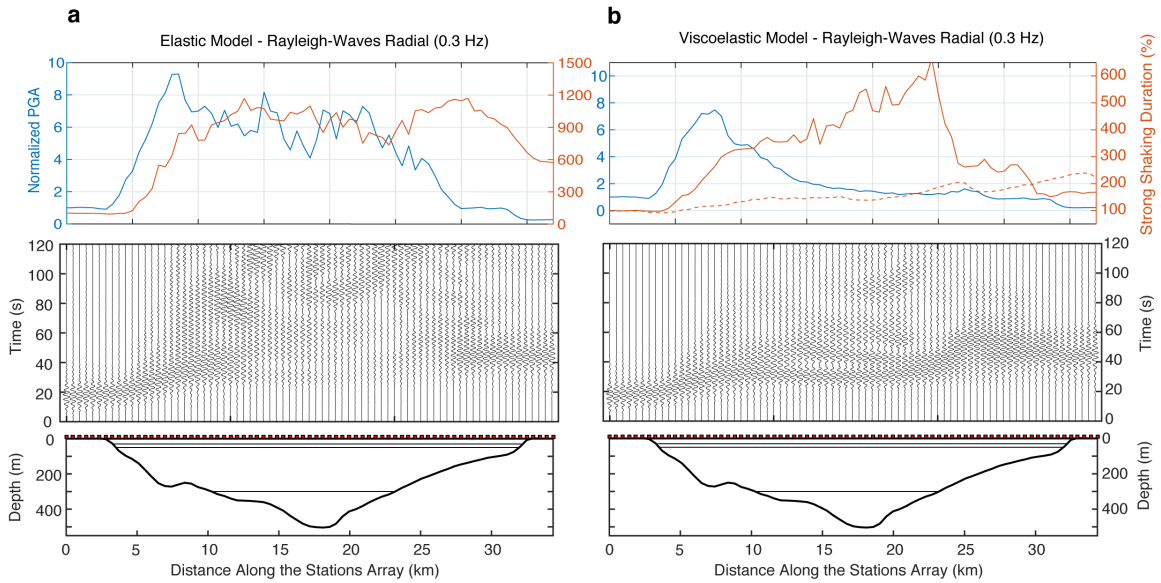

Figure A7 Same as Figure 5 but for f = 0.3 Hz.

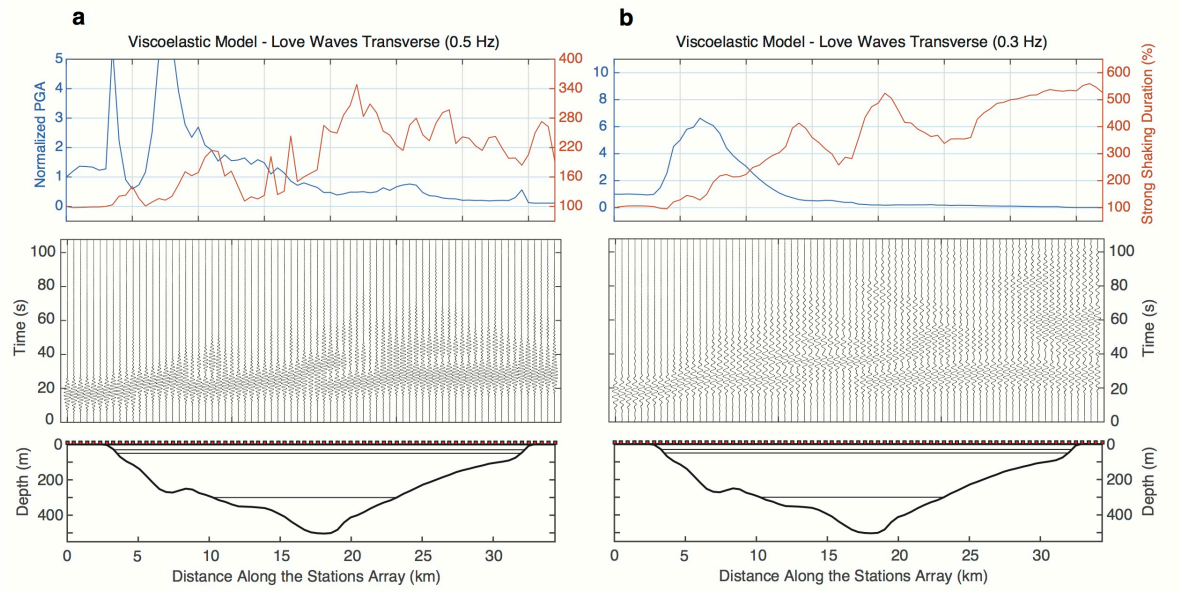

Figure A8 Same as Figure 5 but for Love waves in the viscoelastic model at (a) f = 0.5 Hz and (b) f = 0.3 Hz. This simulation corresponds to a 1.5 km depth double-couple strike-slip point source at location S6.

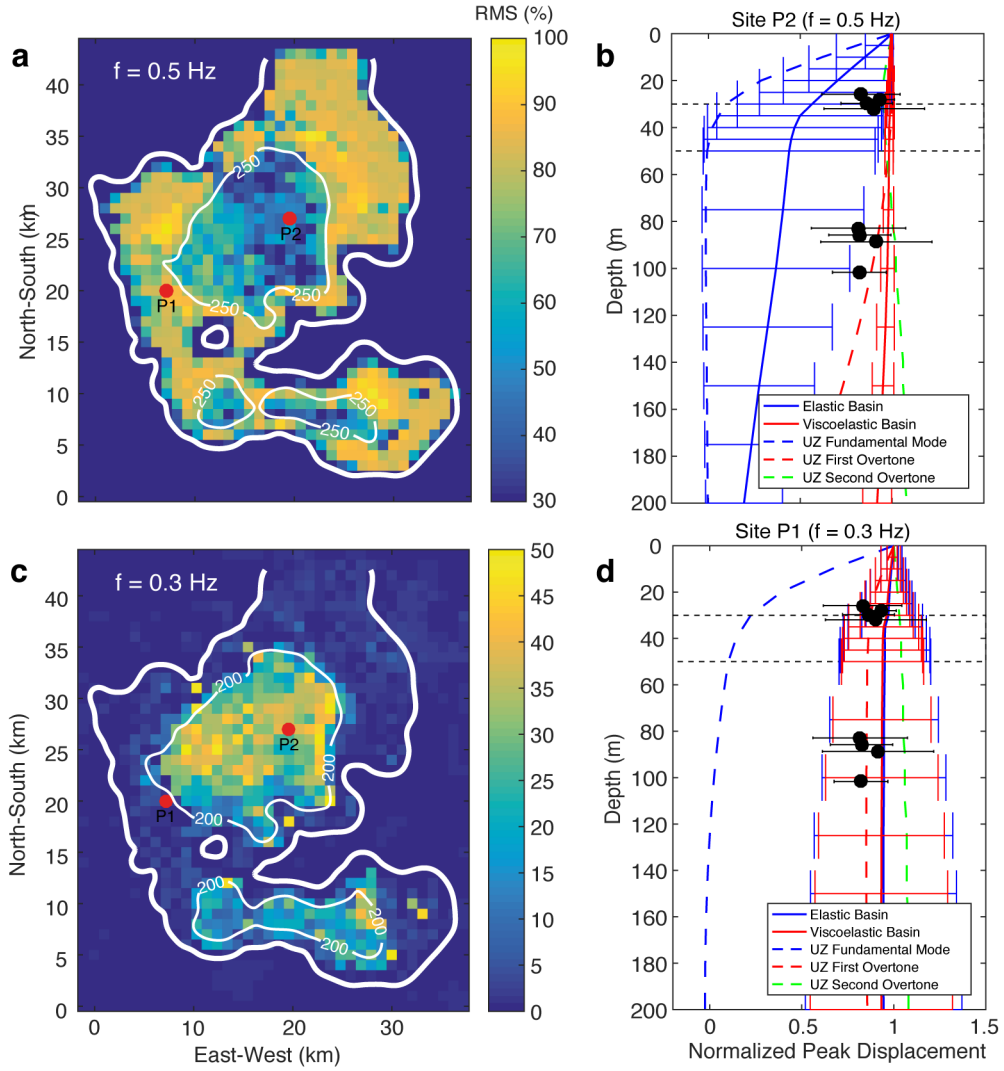

Figure A9 (a) and (c) RMS differences of the averaged (for the eight sources) elastic and viscoelastic eigenfunctions computed in the whole borehole network shown in Figure 1 for two different frequencies. White contours delineate the basin geometry at fixed depths in meters. Yellow colors depict regions where attenuation plays a major role resulting in the dominance of Rayleigh waves first overtones. (b) and (d) Same as Figure 6 but for frequencies of 0.3 and 0.5 Hz at representative sites P1 and P2. Notice the dominance of first overtones at 0.3 Hz for both elastic and viscoelastic models in shallow basin regions (i.e., at P1). This figure has been created using the Matlab software Version R2016a, http://www.mathworks.com/.

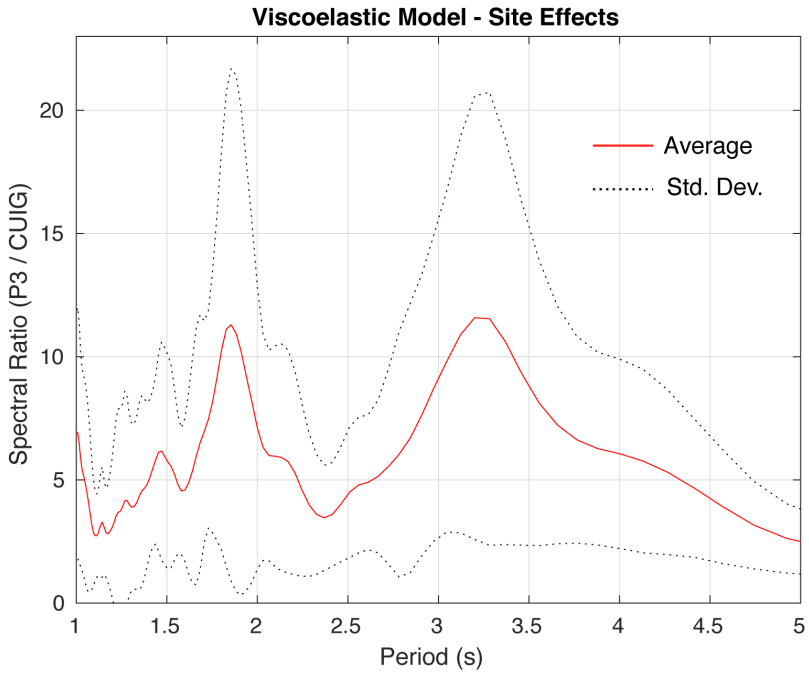

Figure A10 Average horizontal spectral amplification for the eight sources (solid red line) and standard deviations (black dotted lines) at the lake-bed representative site P3 (Figure 6) with respect to the hard-rock CUIG site.

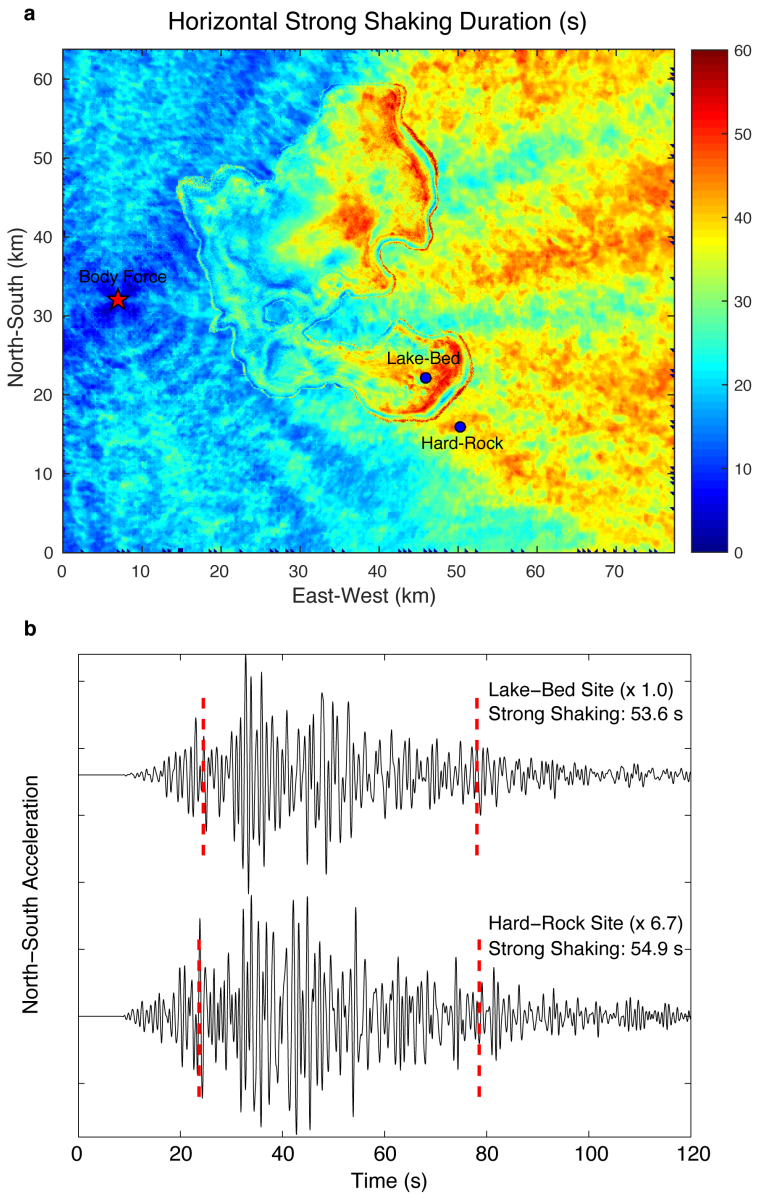

Figure A11 (a) Duration of the strong shaking phase of the Green's function due to source S6 (Figures 1 and 4) averaged for both horizontal components and f < 1 Hz. Notice the long duration of ground motions in both the sedimentary basin and the external shadow region. (b) Seismograms computed in two close sites, one in the lake-bed zone and the other at hard-rock within the seismic shadow. Red dashed lines indicate the strong shaking phase computed form the Arias intensity. Although very different in amplitude, durations of their strong phases are almost the same. This figure has been created using the Matlab software Version R2016a, http://www.mathworks.com/.